3-11-2011

Development of an interference lithography capability using a helium cadmium ultraviolet multimode laser for the fabrication of sub-micron-structured optical materials

Stanley D. Crozier

DEVELOPMENT OF AN INTERFERENCE LITHOGRAPHY CAPABILITY USING A HELIUM CADMIUM ULTRAVIOLET MULTIMODE LASER FOR THE FABRICATION OF SUB-MICRON-STRUCTURED OPTICAL MATERIALS

THESIS

Stanley D. Crozier Jr., 2nd Lieutenant, USAF

AFIT/GE/ENG/11-07

DEPARTMENT OF ELECTRICAL AND COMPUTER ENGINEERING

AIR FORCE INSTITUTE OF TECHNOLOGY

Wright-Patterson Air Force Base, Ohio

AFIT/GE/ENG/11-07

DEVELOPMENT OF AN INTERFERENCE LITHOGRAPHY CAPABILITY USING A HELIUM CADMIUM ULTRAVIOLET MULTIMODE LASER FOR THE FABRICATION OF SUB-MICRON-STRUCTURED OPTICAL MATERIALS

THESIS

Presented to the Faculty

Department of Electrical and Computer Engineering

Graduate School of Engineering and Management

Air Force Institute of Technology

Air University

Air Education and Training Command

In Partial Fulfillment of the Requirements for the

Degree of Master of Science in Electrical Engineering

Stanley D. Crozier Jr., B.S.E.E.

2nd Lieutenant, USAF

March 2011

AFIT/GE/ENG/11-07

DEVELOPMENT OF AN INTERFERENCE LITHOGRAPHY CAPABILITY USING A HELIUM CADMIUM ULTRAVIOLET MULTIMODE LASER FOR THE FABRICATION OF SUB-MICRON-STRUCUTURED OPTICAL MATERIALS

Stanley D. Crozier Jr., B.S.E.E.

2nd Lieutenant, USAF

Approved:

Michael A. Marciniak (Chairman)	15 Mar 11 Date
Michael Havrilla Michael J. Havrilla (Member)	15 Mar 11 Date
Ronald A. Coutu Ronald A. Coutu, Jr. (Member)	15 Mar 11 Date

Abstract

Interference lithography (IL) is an alternative photolithography method to standard masking techniques used to fabricate semiconductor devices. In photolithography, a patterned mask or template creates periodic structures in integrated circuits (ICs) and can take considerable time to fabricate on a large scale. Rather than using a conventional mask, IL directly exposes an interference pattern created from the superposition of multiple laser beams to generate patterned layers within a semiconductor device. The benefits of IL include single-step processing, large-scale pattern fabrication, and the creation of defect-free structures. The goal of this work is to develop unique holograms on semiconductor-metal thin films to characterize as potential optical metamaterials. This is achievable by developing a fabrication recipe to include exposure methods, exposure dosages, and material development. This study developed an IL capability at AFIT for the first time with period resolution below 230nm. It also identified initial acceptable photoresist materials and exposure dosages, and a path to follow to optimize this process. The potential impact of this is to make IL a standard in optical metamaterial fabrication, which decreases manufacturing time and allows for less error in production. These aspects support a variety of Air Force applications, including high efficiency solar cells and spacecraft thermal management.

Acknowledgements

I would like to express my sincere appreciation to my academic and research advisor, Dr. Michael Marciniak, for his guidance and support throughout the course of this effort. The insight and experience was certainly appreciated. I would also, like to thank my sponsor, Dr. Augustine Urbas, from the Materials and Manufacturing Directorate at the Air Force Research Laboratory for both the support and latitude provided to me in this endeavor.

I am also indebted to the many maintenance professionals who spent their valuable time explaining the processes and procedures they used in the maintenance of their support equipment. Special thanks go to Mr. Paul Cassity, who was my liaison and was always available to answer my questions.

Stanley D. Crozier Jr.

TABLE OF CONTENTS

List of Figures

Figure Page

List of Abbreviations

DEVELOPMENT OF AN INTERFERENCE LITHOGRAPHY CAPABILITY USING A HELIUM CADMIUM ULTRAVIOLET MULTIMODE LASER FOR THE FABRICATION OF SUB-MICRON-STRUCUTURED OPTICAL MATERIALS

I. Introduction

The objective of this thesis is to investigate optical lithography as a standard method for the fabrication of optical metamaterials. Optical metamaterial devices affect the electric and magnetic fields through capacitive- and inductive-like nanostructures. Polarimetric scatterometry is an optical technique practiced at AFIT to characterize the bidirectional transmission and reflection of light incident upon a sample. This type of characterization combined with a fabrication method can lead to developing materials not found in nature that possess unique optical properties. However, this process is limited by the AFIT's inability to fabricate metamaterial samples in house. The capability to fabricate metamaterials in house would eliminate reliance on outsourced samples. By implementing optical photolithography, AFIT can attain self-sufficiency by optimizing in-house metamaterial fabrication, thus advancing characterization research by increasing sample throughput.

The goal of this research was to explore the capabilities of manufacturing metamaterial samples with equipment currently in place. Results with the equipment will allow the characterization research to move forward without the dependence of outsourcing optical meta-materials.

1.1 Importance of Interference Lithography

"Since the beginning of the microelectronics era, the minimum feature length of an integrated has been reduced at a rate of about 13% per year and will have reached 50nm by the year 2010 [13:8]." As technology has ascended into the 21st century, electronic devices have become smaller in scale than in previous years. So far, this trend has stayed true to Moore's Law, which states that the number of transistors manufactured onto chips doubles every two years. This is due in part by the approaches of lithographic processes to construct optical circuitry at the nano-scale. Nano-scale accessibility has become increasingly important in the areas of physics and chemistry for advances in nanotechnological development. The importance of the new science involves increased surface/volume ratio and quantum phenomena. The semiconductor industry has well-established optical lithography as the manufacturing choice for fabricating integrated circuit (IC) technology. Optical lithography traditionally incorporates a mask-based technique into constructing microstructure circuitry [2]. In photolithography, a photosensitive material called photoresist (PR) coated on substrate material is exposed to a monochromatic light source through a mask. The mask, which contains geometric shapes transfers to the PR layer and represents only one level of IC design. The mask image defines various regions of an IC, but resists patterns are only replicas and are a representation of the circuit features in a final device. To produce permanent circuit features, an etching process transfers the patterns into underlying layers comprising a device. The etching process selectively removes unmasked portions of a layer to transfer the pattern. The entire process with additional p-n junction fabrication steps is shown in further detail in Figs. 1.1 and 1.2

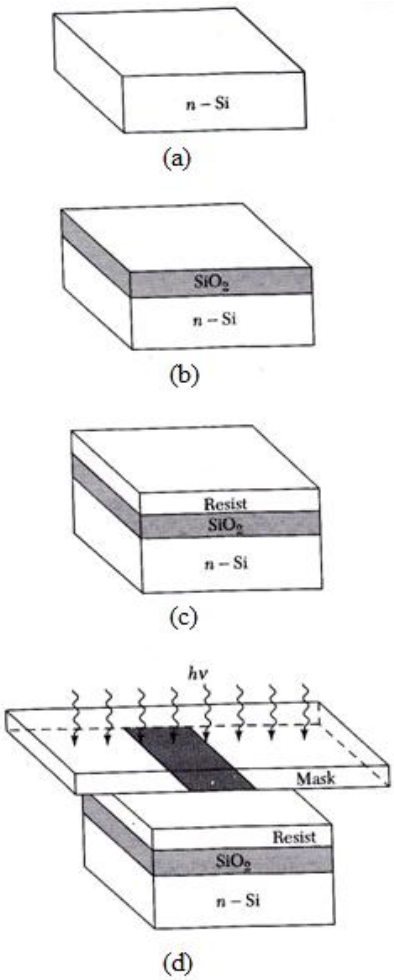

Fig. 1.1 Beginning photolithographic stages of p-n junction fabrication. (a) An n-type Si substrate wafer. (b) An oxidized Si wafer. (c) The application of PR on top of the oxidation layer. (d) PR exposure through the mask [13:12].

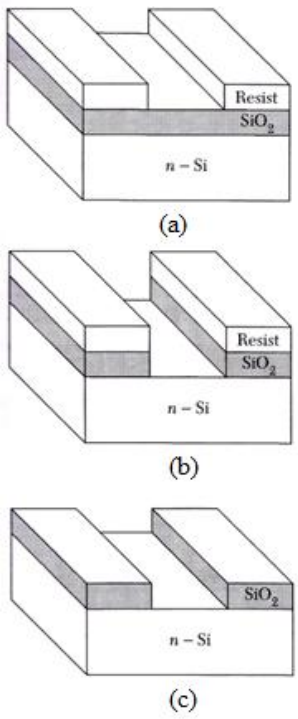

Fig. 1.2 Final stages of p-n junction fabrication. (a) The Si wafer after the PR has been developed. (b) SiO_2 removal. (c) The final results after a complete lithographic process. [13:13].

Another technique for optical lithography that does not use a traditional mask-based exposure and instead creates microstructures by light interference is interferometric lithography. The advantages of interferometric processes include one-step large area recording and defect-free processing [14]. These interference patterns can be manufactured to create highly functional two-dimensional (2D), or three-dimensional (3D) structures by controlling beam properties, such as amplitude, phase, wave vector, and polarization [19]. However, this approach can introduce

alignment complexity and inaccuracies due to differences in beam coherence length, interference angles, and instabilities from free flowing vibrations within an optical setup [8].

1.2 Motivation for Interference Lithography

Currently, there is no fabrication recipe here at AFIT to develop metamaterial devices with IL techniques. AFIT does however have the capability to characterize metamaterials to gain knowledge about their unique optical properties. These types of characteristics represent a small but significant step within the grand scheme of engineering technology that is highly energy efficient. By designing a photolithography method specific to constructing certain kinds of metamaterials, it will then be possible to make considerable advancements through knowledge gained to revolutionize optical devices.

1.3 Organization

This thesis is organized as follows:

- Chapter II: An overview of interference lithography definition, development, and applications.
- Chapter III: An overview of the equipment, measurement methods, and procedures used in this effort.
- Chapter IV: Results and Discussion of the documented measurements.
- Chapter V: Conclusion and further recommendations for the development of in-house fabrication with interference lithography.

II. A Physical and Mathematical Understanding of Interference Lithography and Its Application for Novel Optical Materials

This chapter introduces definitions and the mathematical development of optical interference for implementation into photolithography processes. The progression of the information focuses on several exposure tools designed to create interference. This chapter looks at each of their technological advantages and limitations for optical lithography. Next, a discussion on current work in photolithography will show the performance of different lithographic systems that use various fabrication techniques. Finally, this chapter will conclude by describing the potential applications of the current optical devices created from interference lithography.

2.1 Interference

Interference is two or more light waves superimposed to yield a resulting light wave whose irradiance differs from the sum of their individual irradiances. There are many common manifestations of the interference phenomenon. For example, rough circular color patterns from sunlight shinning across an oil slick or the interaction of surface ripples in a pool of water (Fig. 2.1). The light and dark zones on the surface of the water represent the maxima and minima of interference, respectively. These types of patterns are interference fringes [11:385].

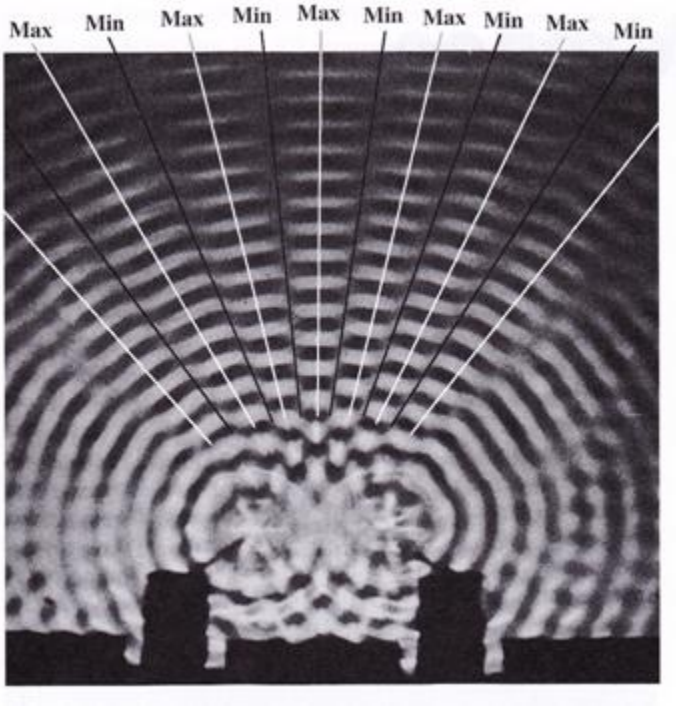

Fig. 2.1 Water waves from two in-phase point sources in a ripple tank. The waves represent interference fringes of maximum and minima [11:386].

Although light interference can take many forms, there are certain conditions that must be met in order to replicate interference with beams of light. For instance, a stable interference pattern can only be produced if the light beams are very near the same frequency. With that said, white light can still produce observable interference due to the elemental colors interfering. Reds will interfere with reds, and blue with blues until the overlapping monochromatic patterns produce a single total white-light pattern. The highest resolution patterns occur when the interfering light waves have equal or nearly equal amplitudes. A resulting contrast of the maxima and minima of the interference fringes corresponds to constructive and destructive

interference, respectively. Lastly, for a fringe pattern to be observed, the interfering light sources must be coherent, or otherwise, the result is a shifted pattern from a phase shift difference within the interference pattern [11:390].

2.2 Wavefront-Splitting Interferometers

The dilemma in producing interference of two or more light sources is that they must be coherent. Other than the use of a laser, no means exist for combining two separately independent coherent sources to generate interference. To solve this problem, a method was developed by Dr. Thomas Young to produce interference in which light from a single source was separated into two light waves and then recombined. Young's experiment, depicted in Fig. 2.2, superimposed cylindrical waves from a double-slit aperture to produce constructive and destructive interference from a single source [11:393].

The following equations were derived from *Optics Fourth Edition* in Ch. 9 and explain the geometry of interference for Young's experiment [11:393-396]. Constructive interference for Young's experiment will occur when

$$r_1 - r_2 = m\lambda \tag{1}$$

where $r_1$is the path of difference of B to P in Fig. 2.2(c), r_2 is the path difference of S_2 to P, *m* is the *m*th order of the interference maximum, and λ is the source light wavelength.

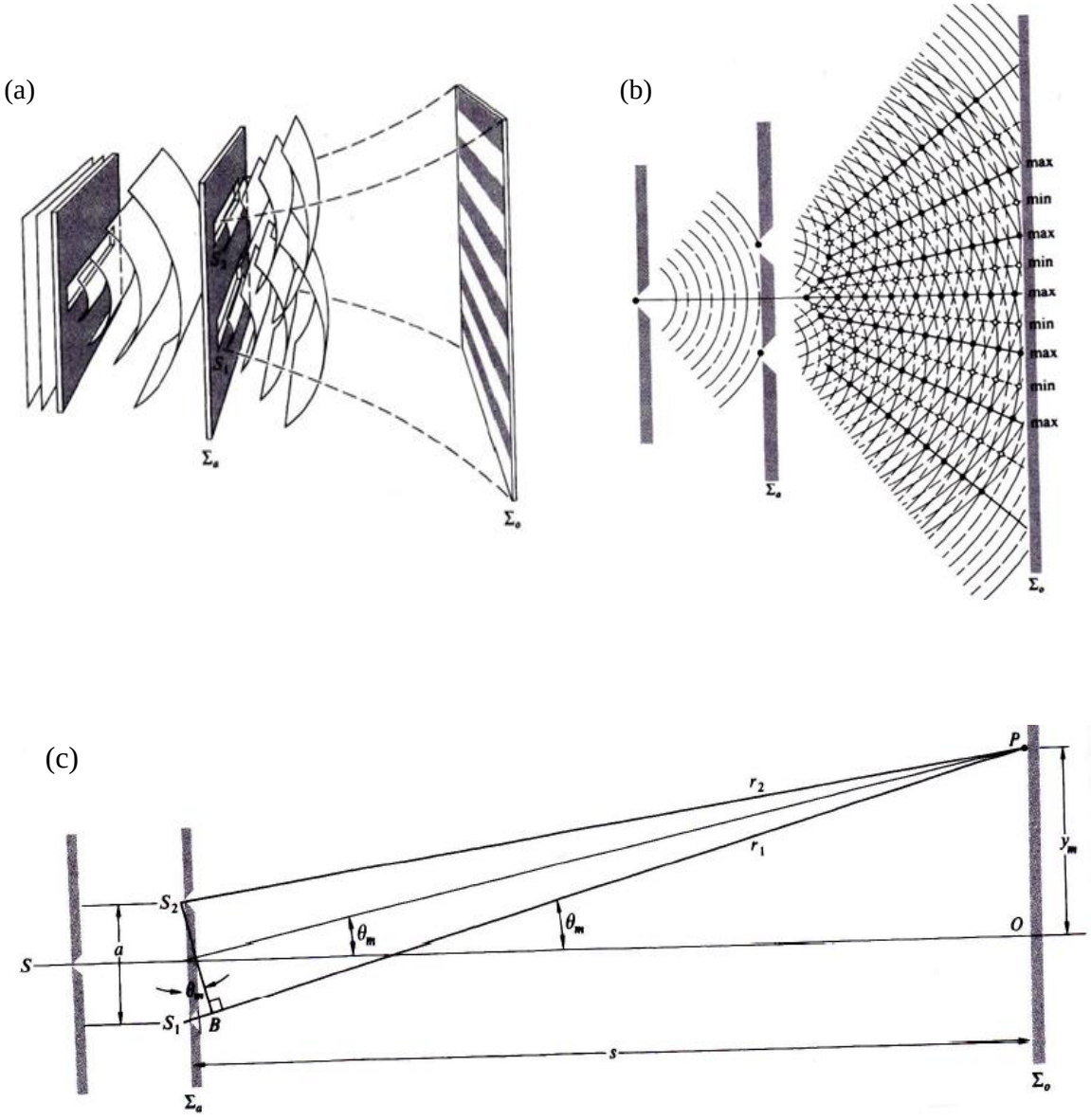

Fig. 2.2 Young's Experiment. (a) Cylindrical waves superimposed in the region beyond the aperture screen. (b) Overlapping waves showing peaks and troughs. (c) The geometry of Young's experiment [11:394].

Then, the position of the *m*th bright fringe is obtained through

$$y_m \approx \frac{s}{a} m\lambda \tag{2}$$

where y_m is the distance of the *m*th bright fringe and the center of the slits, *O*, *s* is the distance between the aperture screen and the double slits, and *a* is the period of slits S_1 and S_2. The angular position of the fringe is

$$\theta_m = \frac{m\lambda}{a} \tag{3}$$

The spacing of the fringes and the difference in the positions of the two consecutive maxima is

$$\Delta y \approx \frac{s}{a} \lambda \tag{4}$$

Since the interference pattern is equivalent to that for two overlapping spherical waves

$$I = 2I_o(1 + cos\delta) = 4I_o cos^2 \frac{\delta}{2} \tag{5}$$

where *I* is the interference irradiance, I_o is peak irradiance, and δ is the phase difference.

Using the phase difference

$$\delta = k(r_1 - r_2) \tag{6}$$

where *k* is the magnitude of the wave vector. In combination with equation (5), *I* can be rewritten as

$$I = 4I_o cos^2 \frac{k(r_1 - r_2)}{2} \tag{7}$$

given that the beams are coherent and have equal irradiances, I_o.

With

$$r_1 - r_2 \approx \frac{ya}{s} \tag{8}$$

the resultant irradiance becomes

$$I = 4I_o cos^2 \frac{ya\pi}{s\lambda} \tag{9}$$

2.2.1 Lloyd's Mirror

Among only a few other interferometers, the Lloyd's mirror relates to the same physical and mathematical considerations as Young's experiment. Also, a wave-front-splitting interferometer, the Lloyd's mirror consists of either dielectric or metal that serves as a mirror, from which a portion of a source cylindrical wave front from slit *S* (as in Fig. 2.3) is reflected and made to interfere with the portion of the incident wave that directly proceeds to the aperture screen from the source. The conceptual arrangement of the Lloyd's mirror is depicted in Fig. 2.3 to show how the fringe pattern is complementary to that of Young's experiment. A distance, *a*, is the separation of the two coherent light sources at the actual slit and its image S_1 due to the mirror. The spacing of the fringes is again $(s/a)\lambda$. The following equations explain the interference geometry for the Lloyd's mirror [11:399].

The reflected beam of this device at incidence ($\theta_i = \pi / 2$) undergoes a 180° phase shift and an additional phase shift of $\pm\pi$ gives,

$$\delta = k(r_1 - r_2) \pm \pi \tag{10}$$

and the irradiance becomes

$$I = 4I_o sin^2 \frac{ya\pi}{s\lambda} \tag{11}$$

The phase shift in the Lloyd's mirror gives a fringe pattern of maxima and minima that exist in the opposite of Young's double-slit device [11:399]. Another design configuration of the Lloyd's mirror is illustrated in Fig. 2.4. This setup uses a monochromatic light source to make interference fringes with period of

$$P = \frac{\lambda}{2sin\theta} \tag{12}$$

where λ is the laser wavelength, and θ is the incident angle upon which laser light reflects from the mirror onto a viewing screen [3].

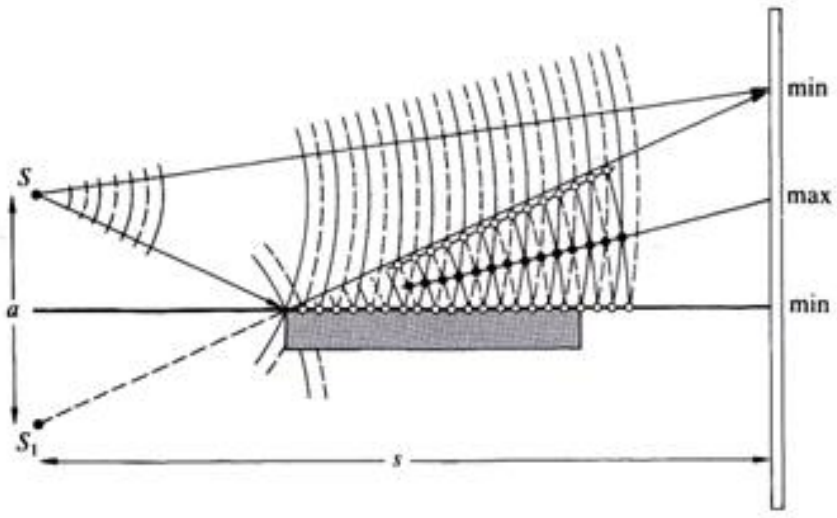

Fig. 2.3 The Lloyd's mirror schematic [11:399].

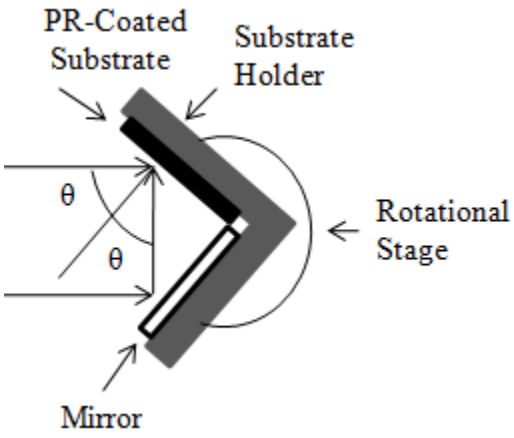

Fig. 2.4 Lloyd's mirror interferometer.

As the incident angle of the reflected beam increases, the fringe spacing decreases causing the optical path difference (OPD) (shown in Fig. 2.5) to change, therefore, decreasing the mutual coherence of the interfering beams [3]. A decreased coherence also limits the visibility of the interference fringes. Visibility, V, for a uniform Lloyd's mirror produced interference pattern is defined as

$$V = \frac{D_{MAX} - D_{MIN}}{D_{MAX} + D_{MIN}} \tag{13}$$

where D_{max} and D_{min} are the maximum and minimum values of the sinusoidal distribution of the inferring beams.

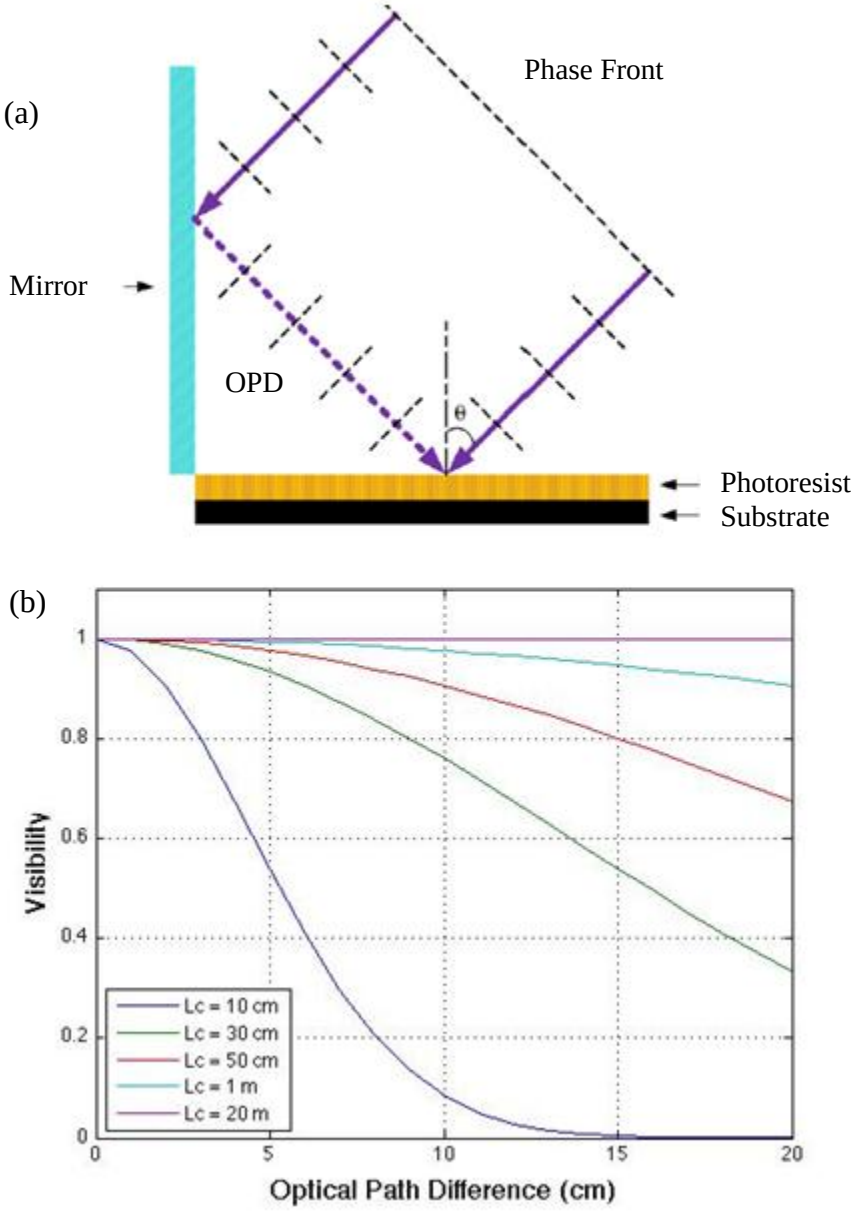

Fig. 2.5 Optical path Difference (OPD) (a) in the Lloyd's mirror interferometer and (b) visibility as a function of coherence length L_c [3].

The visibility can also be written is terms of the coherence length, L_c, of the source laser and the OPD in the following equation:

$$V = \exp\left[-\left(\frac{\pi * OPD}{2L_c}\right)^2\right] \tag{14}$$

Fig. 2.5(b) shows the fringe visibility plotted against OPD for various laser coherence lengths. The data for laser light with the shortest coherence length has as unstable fringe visibility for an increasing OPD. As shown for the plot of L_c = 20m, only a laser beam with a coherence length greater than one meter is the fringe visibility stable across a large OPD [3].

2.3 Amplitude-Splitting Interferometer

Amplitude-splitting is a technique in which light is partially reflected into separate parts, transmitted into different directions, and then recombined upon a surface to produce interference. The concern with this type of interferometer is the ability to keep the separated light from traveling an optical path difference that does not exceed the coherence length of the source light. If the path lengths of the separated beams differ by a distance greater than the coherence length of the light, then the recombined portions to create interference would correspond to different wave groups. At this point, the interference would be unstable due to a nonexistent common phase relationship between the beams, therefore yielding an unobservable fringe pattern [11:400].

A Michelson interferometer utilizes an arrangement of mirrors and beam splitters to produce interference by means of amplitude-splitting. Its optical configuration is illustrated in Fig. 2.6.

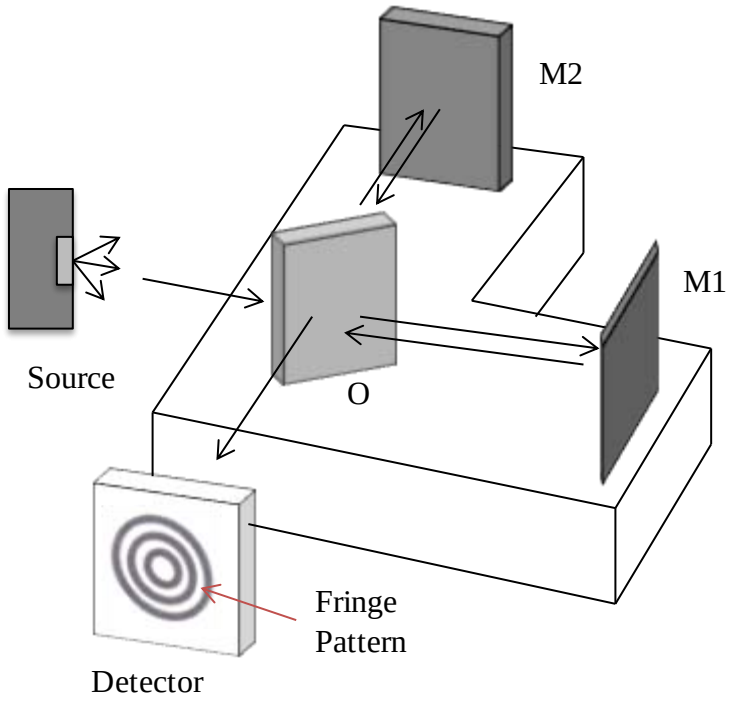

Fig. 2.6 The Michelson interferometer [11:408].

An emitting monochromatic source transmits light waves to a beam splitter at position *O*, which divides the wave in two. The beam splitter is oriented at a 45° angle to direct the split waves orthogonally towards mirrors *M1* and *M2*. The two waves are then reflected by *M1* and *M2* back towards the beam splitter at *O*. Once the waves have returned to position *O*, the beam splitter then channels the reflected beams from *M1* and *M2* for recombination at the detector aperture. The overlapping beams at the detector produce an interference pattern of circular fringes known

as Newton's rings [11:407-410]. Reference *Optics Fourth Edition* Ch. 9 pages 407 - 410 for an understanding of how the Michelson creates interference fringes.

2.4 Interference Lithography

Interference lithography (IL) is an optical fabrication technique used for transcribing an interference pattern into photosensitive material. This technique has emerged as a fabrication process for semiconductors and other IC devices using two or more coherent laser beams to produce large areas of periodic interference patterns. The period of the interference pattern is dependent on the incident angle of the beams and the wavelength of the source laser light (see equation (12)). As an alternative to photolithographic processes that use masks to transcribe patterns into photosensitive layers, IL is maskless and a more cost effective way to produce holographic shapes. The high-volume potential applications that can be achieved with the use of IL will depend on the limits of uniformity, throughput, process control, and repeatability [10].

IL transfers an intensity distribution from a small number of coherent interfering beams onto a substrate material coated with a photosensitive layer. The intensity distribution, depicted in Fig. 2.7, of the interference of *n* coherent laser beams can be described as

$$I = \sum_{i} E_i^2 + \sum_{i<j} E_i * E_j \cos\left[\left(k_i - k_j\right) * r + \left(\varphi_i - \varphi_j\right)\right], \qquad (15)$$

$$i, j = 1 - n$$

where E_i, $k_{i,j}$, and φ_i denote the amplitude, wave vector, and phase of beam *i*, respectively [14].

(a)

(b)

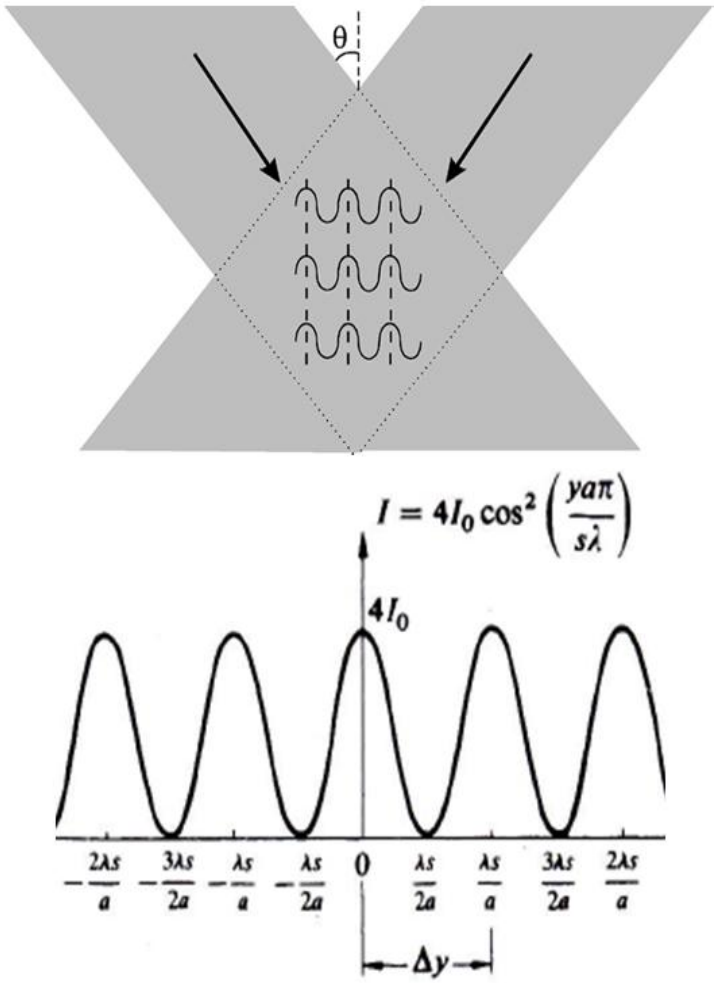

Fig. 2.7 Representation of two-beam interference. (a) Coherent laser beams are symmetrically incident from the left and the right. The period of the interference pattern is $\lambda/[2nsin\theta]$. (b) The standing wave pattern exists throughout the overlap between the beams as long as this overlap distance is shorter than the longitudinal coherence length of the laser beams and the wafer can be placed anywhere inside this coherence volume [2, 11:396].

Photosensitive material, or photoresist (PR), is a radiation sensitive compound that is classified as positive or negative, depending on how it responds to radiation. Each is designed for specific wavelengths of UV light. Since IL applications tend to operate within the UV wavelength spectrum, negative PRs are limited by lower photosensitivity and lower resolution compared to positive PRs. Positive resists become more soluble under exposure, and thus, exposed regions are easily removed during development. For negative resists, the exposed regions become less soluble and bond together after development leaving the unexposed regions to be removed. Both tones have their own chemical properties and react differently to various levels of exposure dosages. For IL, the purpose of PR is to absorb light interference fringes. This occurs when a certain exposure dosage (mJ/cm^2) specific to the PR is met. Once an exposure dose is reached, an interference fringe pattern is developed into the PR by a series of thermal and chemical processes [1]. Fig. 2.8 shows two optical configurations for constructing interference patterns. Fig. 2.8(a) is a Lloyd's mirror arrangement applicable for IL. In this setup, two halves from an incident source beam fold onto each other by 90° geometry [2]. Fig. 2.8(b) is an example of an amplitude splitting interferometer that is useful for source beams that irradiate a beam profile other than a single-mode Gaussian TEM_{00}. Ultraviolet lasers tend to operate at a large number of transverse modes and consequently yield a very low transverse coherence length. A beam splitter, such as an amplitude-spitting interferometer incorporates, provides the necessary capability for self-coherence to produce interference fringes by maintaining both an equal path length and angular relationship [2].

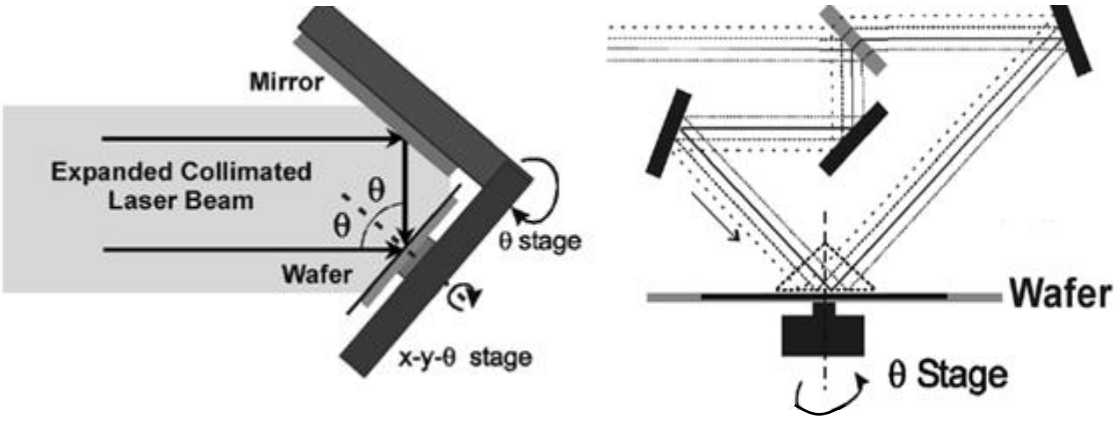

(a) (b)

Fig. 2.8 Experimental arrangements for IL. (a) Lloyd mirror, where the right and left halves of the beam are folded onto each other at a 90° geometry. For lasers that exhibit a large number of transverse modes and have very low coherence, an arrangement shown in (b) maintains small contrast coherence by splitting the beam in half and folding it onto itself [2].

Single-mode TEM_{00} laser sources with a high transverse coherence are successfully used with the Lloyd's mirror interferometer because of their uniform intensity distributions. Fig. 2.9 is a depiction of nanometer PR gratings created from the Lloyd's mirror interferometer which are representative of a Gaussian laser distribution. Transverse Electro-Magnetic (TEM) is a term used to classify the transverse modes of lasers. Each TEM mode describes the cylindrical symmetry of a laser with a specific Gaussian profile. The cylindrical transverse mode patterns shown in Fig. 2.10 demonstrate not all laser beams represent a TEM_{00} mode. For these cases, it is still possible to "clean" higher order beam modes to satisfy a single-mode Gaussian profile with a spatial filter.

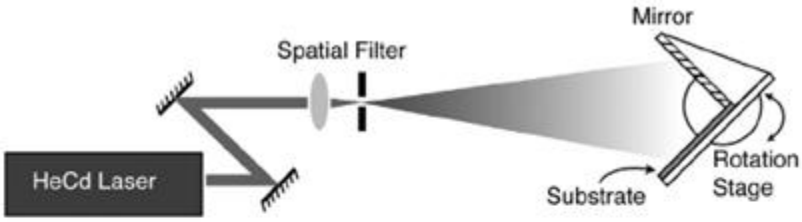

(a)

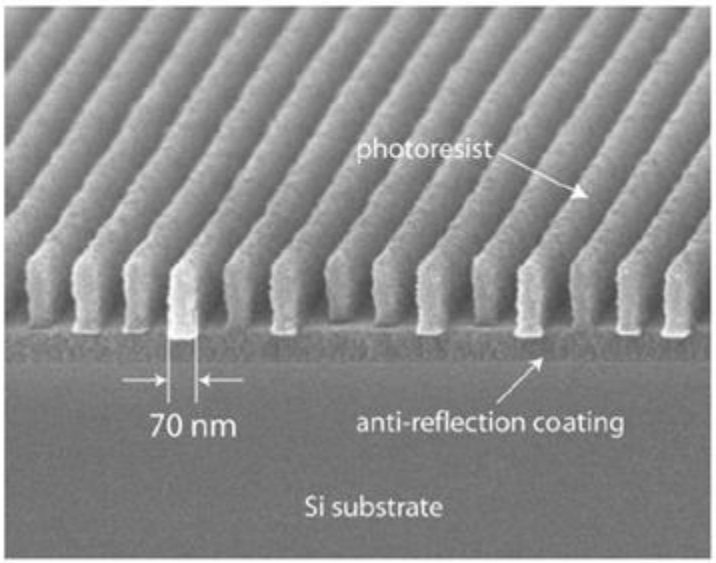

(b)

Fig. 2.9 (a) Schematic of Lloyds mirror interferometer. The substrate and mirror fixed at a 90° angle to one another, centered in a single incident beam. Rotating the substrate/mirror assembly about its center point varies the spatial-period of the exposed grating. (b) The micrograph shows a grating with 70 nm lines on a 170 nm pitch [4].

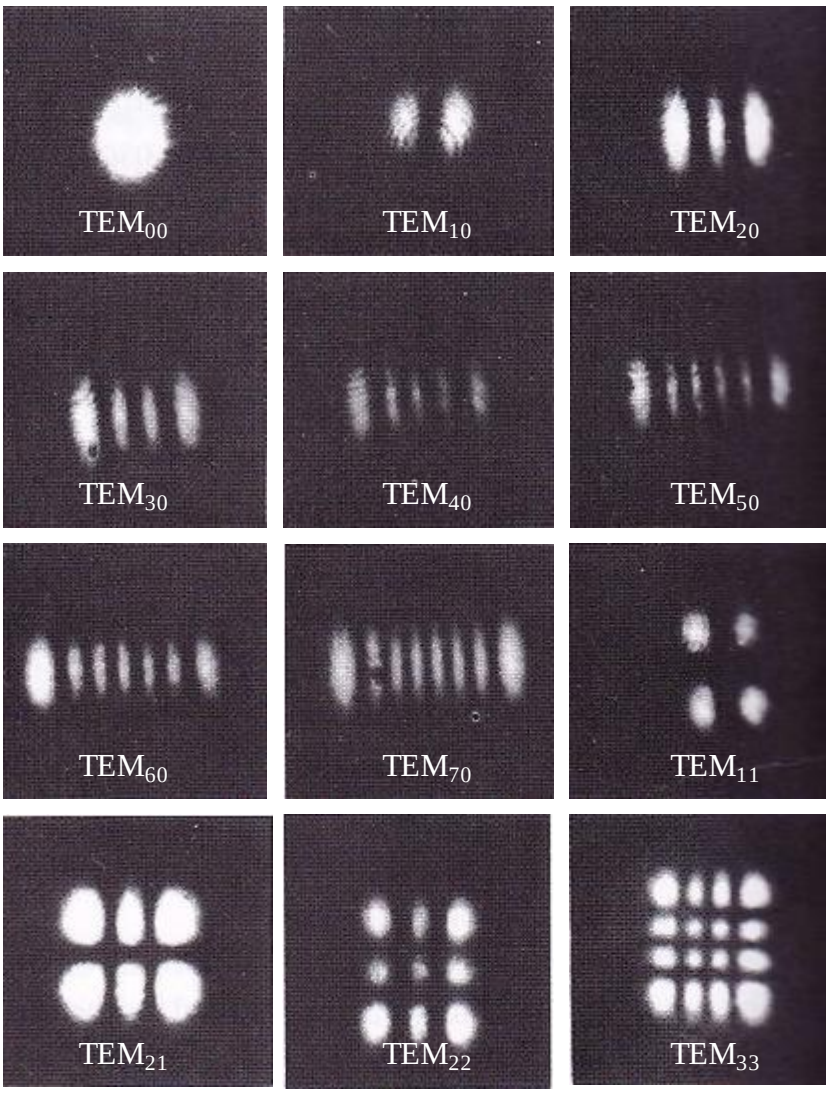

Fig. 2.10 Cylindrical transverse mode patterns [11:592].

A spatial filter is an optical apparatus that allows for an insertion of filters to partially, or completely, block out certain spatial frequencies. This alteration of a frequency spectrum is spatial filtering [11:611]. For example, a spatial filter device consisting of a microscope

objective and a pinhole aperture removes unwanted multiple order energy peaks from a multiple mode laser source (seen in Fig. 2.11). The following equation determines the diameter of the input beam through the pinhole aperture:

$$Beam\ Spot\ Diameter\ (\mu m) = \frac{(2.44 * \lambda * f)}{D} \tag{16}$$

where λ is the laser wavelength (μm), f is the focal length of the objective lens (mm), and D is the input beam diameter (mm). Furthermore, the preferred pinhole diameter from the calculated beam spot size is given by

$$Pinhole\ Diameter\ (\mu m) = 1.5 * Beam\ Spot\ Diameter\ (\mu m) \tag{17}$$

where the *1.5* factor represents the ideal factor for transmitted optimal power through the pinhole aperture while eradicating as much higher mode noise as possible [9].

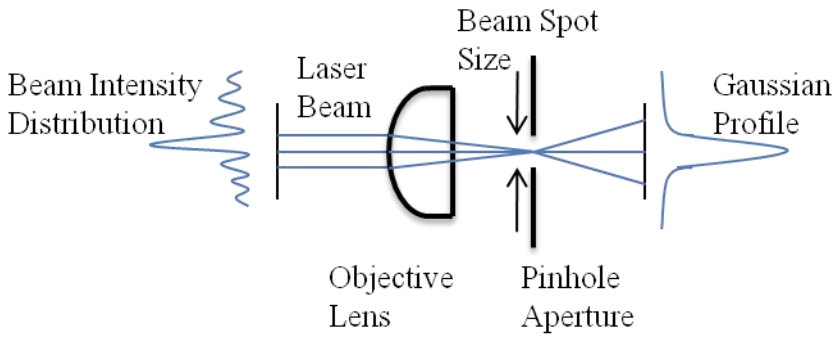

Fig. 2.11 Spatial filter schematic consisting of an objective lens and pinhole aperture [9].

Repetitive arrays, like those in Fig. 2.9(b), have the effect of producing periodic alterations in phase and amplitude to emerging waves, and are referred to as diffraction gratings. Upon reflection from these kinds of gratings, light scattered from the periodic surface features will arrive at a certain point with a definite phase relationship. The consequent interference pattern of maxima generated from reflection is expressed by the grating equation [11:476-477],

$$a * sin\theta_m = m\lambda \tag{18}$$

which is equation (3), but without a small-angle approximation. A more specific approach for the location of *m*th orders is considered in

$$a(sin\theta_m - sin\theta_i) = m\lambda \tag{19}$$

where *m* is dependent on light incidence from the reflecting surface and $\theta_m = \theta_i$ corresponds to the zeroth order, $m = 0$. It is to be noted that this expression is applicable regardless of the refractive index of the grating itself. An illustration of the reflection phase gratings is shown in Fig. 2.12 [11:477-478].

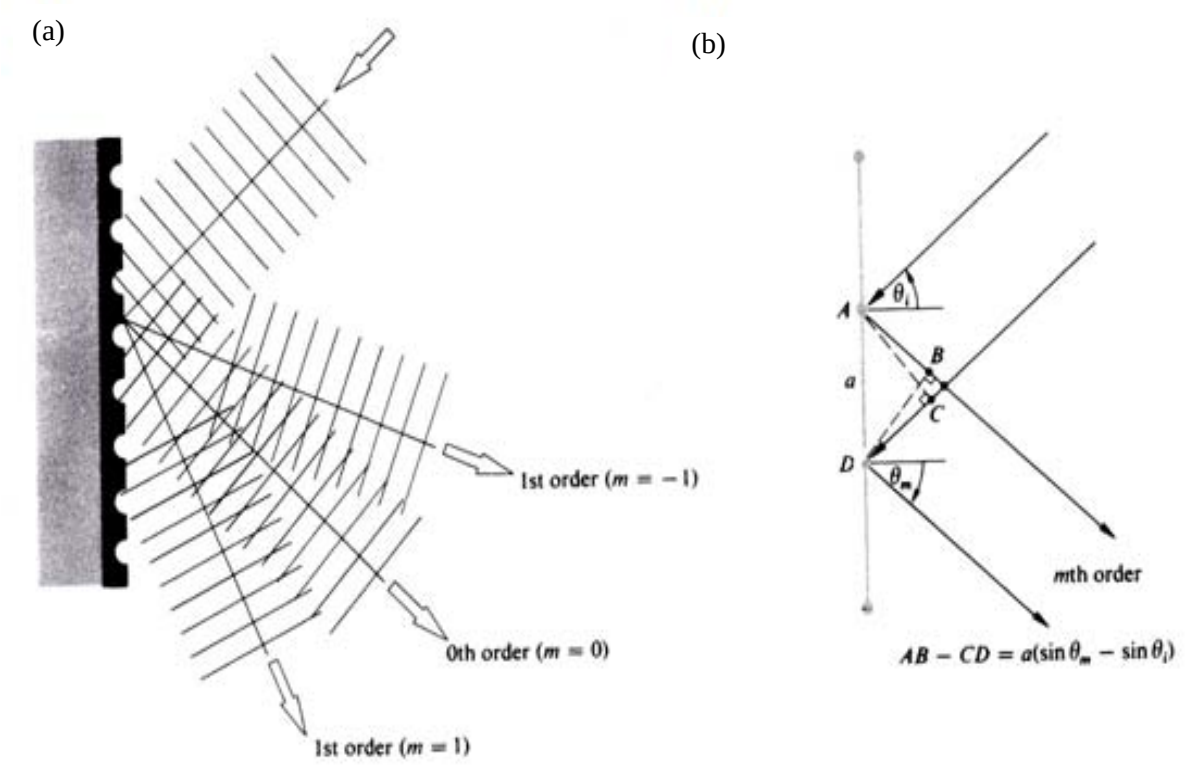

Fig. 2.12 The Reflection Phase Grating. (a) Diffraction orders from the reflection grating. (b) Geometry of the reflection grating included the grating equation [11:478].

2.4.1 Two-Dimensional Interference Patterns

Now that using interference has been established as a means to create periodic fringe arrays in PR, it is also possible to develop those patterns into two-dimensional structures. Constructing two-dimensional structures is not exactly a difficult interference task. For instance, a patterned 2D square array can be produced by two single-shot IL exposures overtop each other with the second exposure performed after a 90° rotation [2]. This is just one of many methods to

demonstrate 2D interference, but the real challenge is PR development which can make producing interference seem like a trivial problem.

Interference fringe orientation, exposure dosages, and resist tone, to name a few, are just some of the problems associated with 2D pattern development and nearly the most essential for producing high-contrast structures. For example, at low exposure doses of a positive tone process, such that an exposure is sufficient to clear the resist during development, holes form where the maxima of the two-interference exposures overlap. For higher doses where the exposure clears the resist, posts form where the minima overlap. The occurrence of holes and posts reverses in negative PRs. To eliminate the need to interchange resist types for hole and post structures, a process known as image reversal produces negative tone images in positive resist. Moreover, image reversal resist structures are produced in the exact opposite sequence for high and low exposure dosages. This process generates high-resolution periods with reduction in process sensitivity and improves resist performance by increasing resist contrast [7]. Interference feature details such as, period consistency, structure depth, and thicknesses of PR layers are sensitive to exposure dosages.

2.5 Applications

This section applies the background information discussed in previous sections to describe the present applications for interference fabrication technology. The focus here is on photonic crystals and plasmonic structures. The purpose of this section is to promote the advantages of IL by showing the significant potential of each device.

2.5.1 Photonic Crystals

A photonic crystal (PC) is a periodic optical structure designed to affect the motion of photons of incident light with a periodic modulation in refractive index comparable to the wavelength of the incident light. This process is similar to semiconductor devices that create energy band-gaps from the flow of electrons. The interest in PC's is the prospect of manufacturing new optical components by fully controlling the existence properties of optical media [14].

In PC's, the interference of the light waves scattered from a crystal lattice leads to photonic band-gaps (PBG's). A PBG is analogous to energy band-gaps in that it acts as an optical conductor by capturing and projecting light into certain directions. The optical properties of a PC with an inclusive PBG provide great interest because of their light redistribution abilities. Refractive index contrast, lattice symmetry, and the capacity of high-index materials all determine the bandwidth and frequency of a PBG. PC's have the potential for advances in various applications including, ultra-high-bandwidth integrated optical circuits, lasers, sensing, spectroscopy, and pulse shaping [15].

IL allows complete control of lattice symmetry for the design of microstructures in a PC [19]. The shape and size of recorded structures are determined by the intensity spectrum of the interference area, as well as by experimental parameters such as PR type, initial PR thickness, developer concentration, contrast of the interference pattern, *etc* [17]. The design of a PC has to contain a threshold intensity surface able to obtain a high contrast pattern [19]. For a multilayered photonic crystal structure, a thick PR, such as the negative-tone SU-8 suffices in fabrication. SU-8 has low absorbance and is highly soluble in the near-UV and visible

wavelengths. High refractive index structured PR can even be used to obtain a PC by doping it with metallic particles or dyes [15]. For example, chemically amplified PRs are typically used in processes where a high liquid-glass transition temperature (T_g) value is desired to achieve submicron resolution in UV lithography. During UV exposure of chemically enhanced SU-8, acids are released in localized regions where a subsequent post-exposure bake accelerates acid diffusion. This is highly undesirable during exposure and ultimately disrupts an interference pattern due to a change in refractive index. A high T_g minimizes acid diffusion during a post exposure bake and facilitates in maintaining a constant refractive index through multiple exposures. Alternatively, loading photosensitizers into a resist film compliments a high T_g by partially neutralizing acid diffusion generated during exposure. Control of acid diffusion, in photolithography, improves resist contrast by photosensitized dyes chemically amplifying the crosslinking of SU-8 [15]. Fig. 2.13 shows the sensitivity curve of photosensitized SU-8 PR as a function of exposure dose from two-beam interference. The sensitivity curves represent the normalized pattern contrast of feature size (d) scaled by the feature distance (p) that is related to both the cross-linking and development dissolution of the PR. As shown, the increasing dosage energy produces a steeper change in crosslinking to create a higher contrast pattern. The slopes of Fig. 2.13 indicate that the SU-8 film loaded with a 0.5wt% H-Nu470 photosensitizer yield the highest contrast pattern. Note that the photosensitive material is particular to visible light, which is appealing in the photolithography of PCs because a longer wavelength allows for a larger lattice period [15].

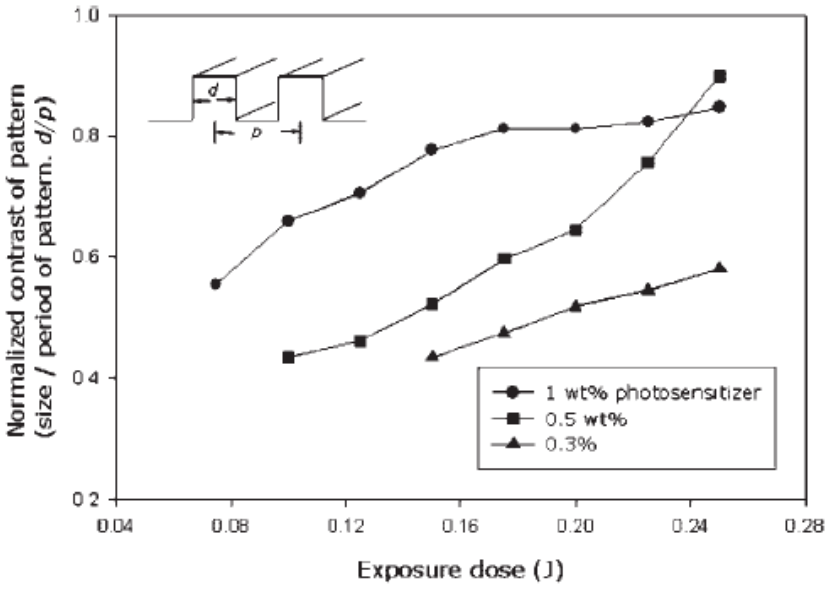

Fig. 2.13 Sensitivity curve of visible SU-8 PR with different loadings of photosensitizers [15].

2.5.1.1 Two-Dimensional Photonic Crystals

Two-dimensional photonic crystals are designed from periodic microstructures on a dielectric medium, which consists of a thin film of high-index refractive material on a low-index substrate [16]. This design enables the ability to control the dispersion of radiation [20]. The structures in Fig. 2.14 represent exposures in positive PR at (a) 90° and (b) 60° to generate columns of cubic and hexagonal lattices, respectively. The construction of these structures follows the scheme in Fig. 2.15.

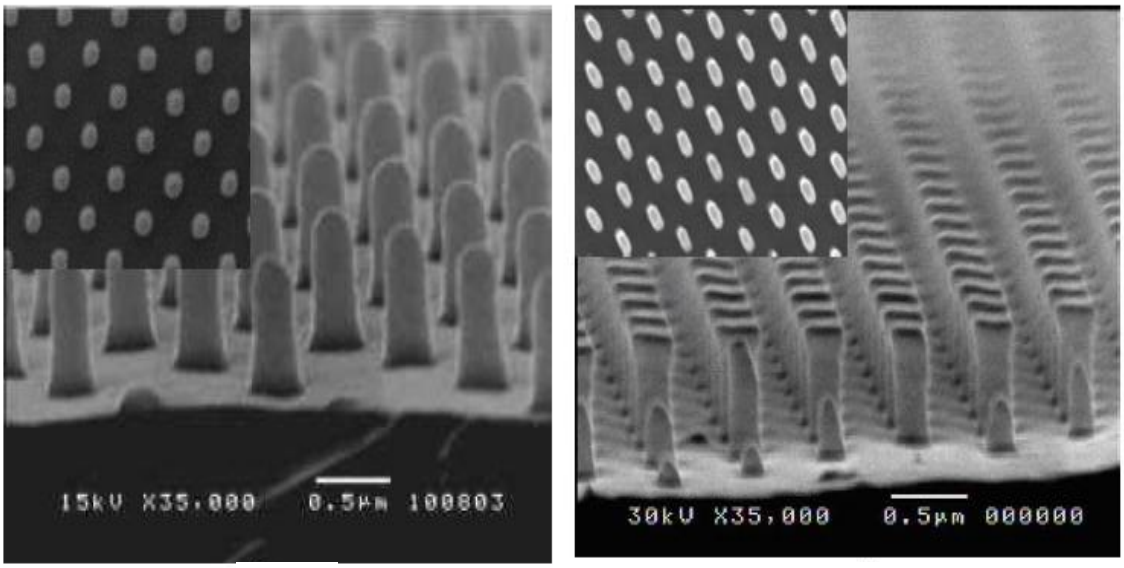

(a) (b)

Fig. 2.14 2D structures recorded by double holographic exposure. (a) Cubic lattice and (b) hexagonal lattice. The size of the scale bar is 0.5µm [17].

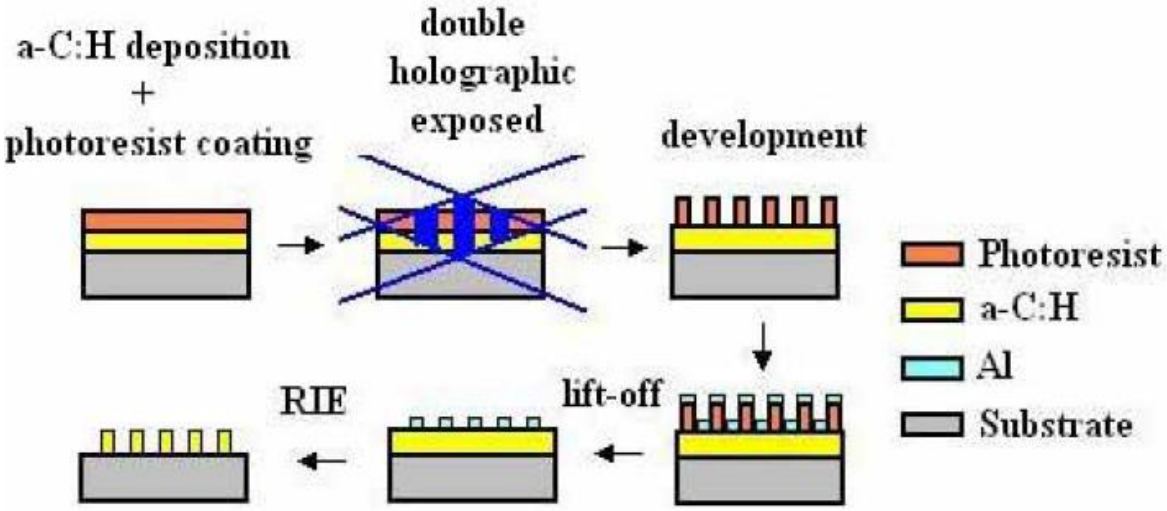

Fig. 2.15 Scheme of the fabrication process for the 2D structures [17].

In this process, resist is spun onto glass substrates with an initial metal deposition and exposed twice with 1D interference fringes. After development, the resist is used as a mask for a metal liftoff process. During the liftoff process, a metal is deposited onto the resist pattern to remove the PR. The remaining metal structure retains the same period and is used as a template for an etch procedure. The final PC shown in Fig. 2.16 is that of columned holes formed from reactive ion etching (RIE) into a a-C:H deposition layer on top of a glass substrate.

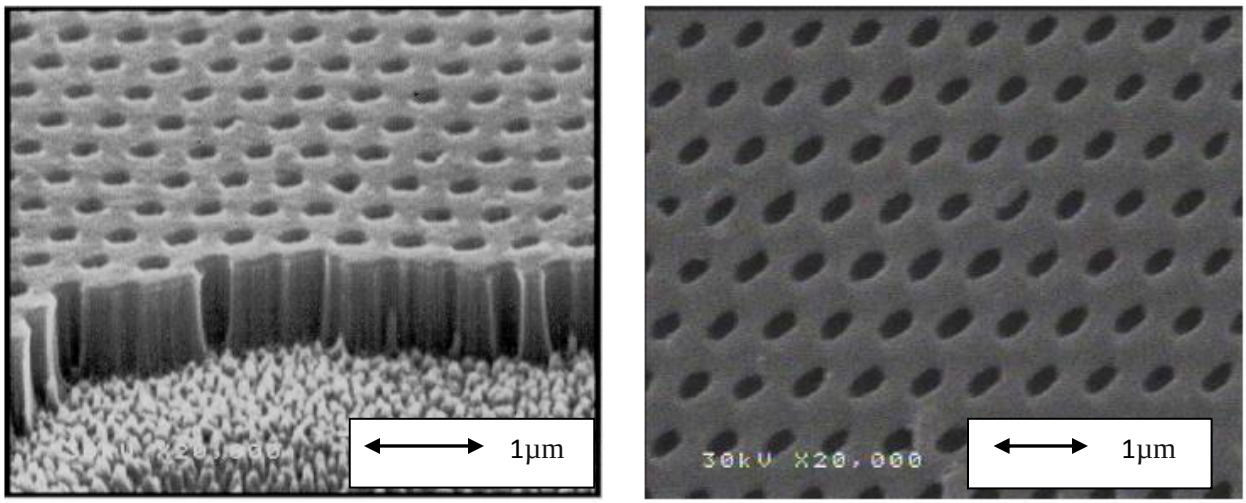

Fig. 2.16 2D structures with hexagonal lattice recorded in a-C:H film. The size of the scale bar is 1μm [17].

A periodic dielectric structure can produce optical band gaps that can be observed in 2D square lattices for designs in passive optical devices [7]. An examination of TE and TM polarization within the constructed lattices can offer insight into optimal device characteristics. Additionally, the band-gap comparisons of the above metal structures make it possible to

determine which pattern has a more significant PBG. Fig. 2.17 shows a calculated PBG graph for the TE and TM polarizations for the two structured PCs. The (r/a) is the ratio of the hole radius, r, and the center-to-center length of the unit cell, a. Observe that the (r/a) limit is 0.5 and 0.67 for the circular and elliptical holes, respectively. For cases in which these values are increased beyond the calculated limits, the dielectric material is represented by columns instead of holes.

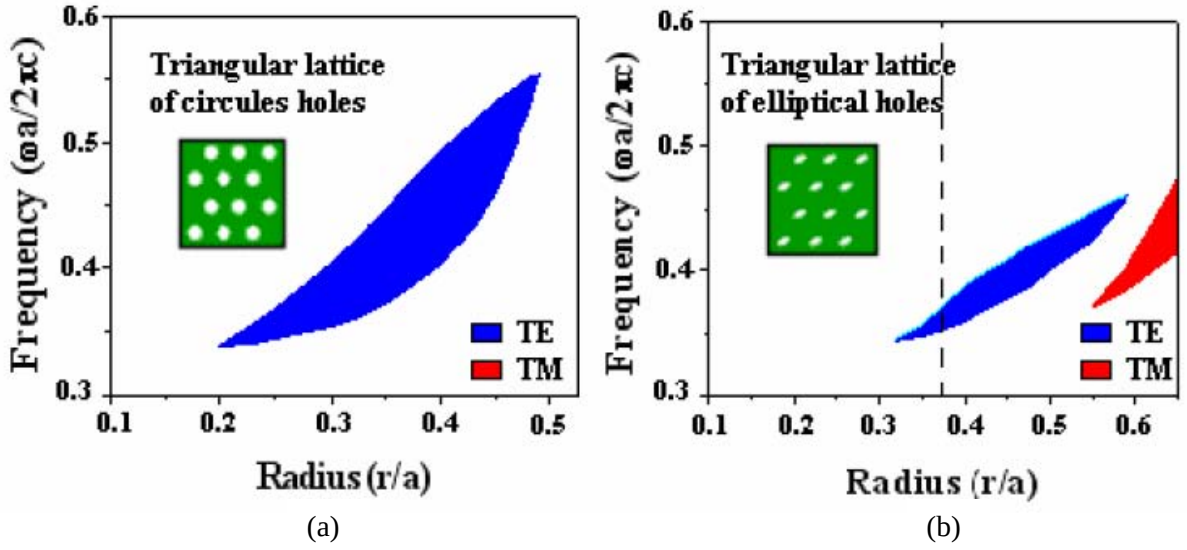

(a) (b)

Fig. 2.17 Gap map for a hexagonal lattices of: (a) circular holes (E=1) and (b) elliptical holes (E=2), in a dielectric material with refractive index n = 2 [17].

The circular holes band diagram of TE polarization exhibits larger PBG areas in comparison with that of the elliptical holes. However, the reduction of the band gap for TE polarization allows for a TM polarization PBG area within the elliptical holes material. Although the PBG area is reduced for the elliptical dielectric structure, it is still capable for the design and

fabrication of hexagonal PC's [17]. Furthermore, the development of 2D PC's is not limited by the IL technique used to create the periodic structures. Using diffractive grating masks for IL, Divliansky *et al.* fabricated a 2D CdSe PC by electrodeposition of CdSe in a polymer template. The PC was synthesized from an initial development of a polymer template produced by exposure of PR by a first-order diffraction pattern created by three-beam interference. The optical arrangement used to create the diffraction pattern, shown in Fig. 2.18, expanded a collimated Nd:YAG laser beam across a mask of three gratings oriented 120° relative to one another. The diffraction mask featured gratings that were 2-μm wide and 4-mm long separated by 2-μm [7].

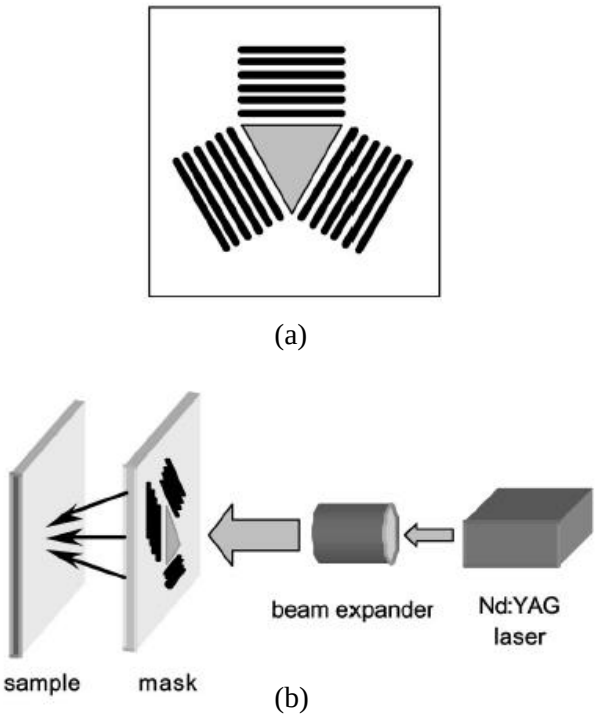

Fig. 2.18 Schematic representation of the (a) three-grating diffraction mask, and (b) optical setup for creating the hexagonal interference pattern [7].

At the focal point of the diffraction pattern, a sample of negative resist was exposed to return a hexagonal array of PR columns with a diameter and period of 1.3 and 2.7μm, respectively [19, 7]. Also, by reducing the dimensions of the gratings and the wavelength of the laser, the band gap can be scaled for visible wavelengths. The scanning electron microscope (SEM) images of the resulting hexagonal array of PR columns and CdSe holes are shown in Fig. 2.19 [7].

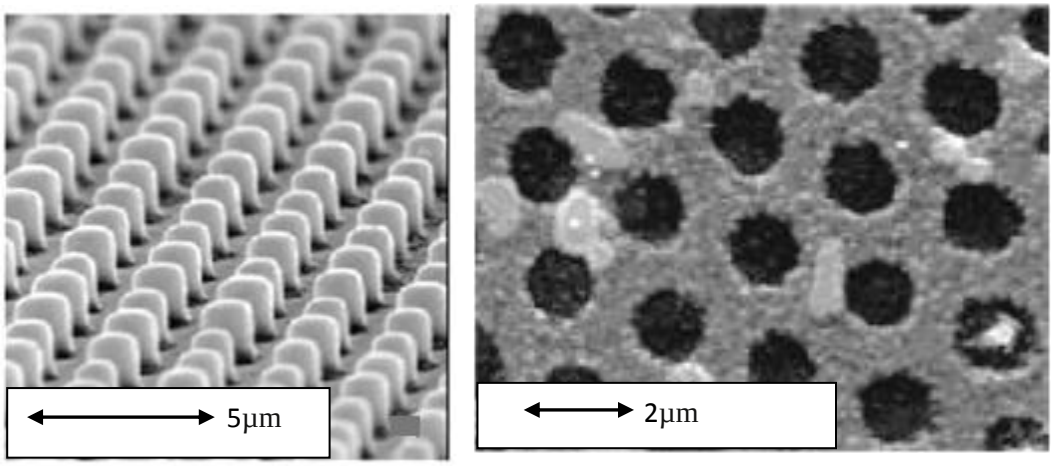

(a) (b)

Fig. 2.19 Optical and SEM images showing the (a) side view of the negative PR columns created by IL, and (b) CdSe PC following CdSe electrodeposition and PR removal. The diameter and pitch of the hexagonal array of air voids are 1.3 and 2.7 μm [7].

Diviliansky *et al*. characterized the CdSe PC using a Bruker Equinox 55 Fourier-transform infrared spectrometer (FTIR) with a mid-infrared source and deuterated triglycine sulfate (DTGS) detector. Fig. 2.20 represents the measured FTIR spectra of the CdSe PC normalized at 0 and 40 degrees to its indium-tin oxide (ITO) coated glass substrate. At a wavelength of 4.23

um and from the measured incident angles, a sharp depression in transmission is observed. As the incident angles increase, the transmission of the CdSe drops and reaches a maximum of 2.6 dB at 40 degrees. A sample of cylindrical air voids was formed in positive PR to accurately mimic the CdSe PC to verify the results. The test sample demonstrated a similar drop in transmission at the same wavelength despite its lower refractive index. This solidified that the drop in transmission resulted from the hexagonal structure with the drop becoming more defined as the contrast of the index of refraction increased [7].

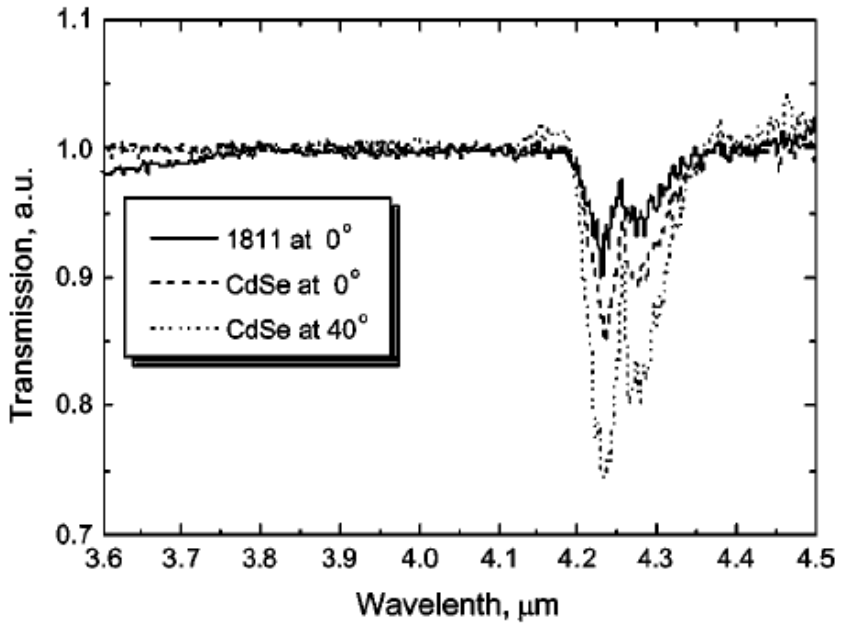

Fig. 2.20 Transmission spectra of CdSe and polymer PCs that have been normalized to the ITO substrate transmission spectrum [7].

2.5.1.2 Sub-Micron Two-Dimensional Photonic Crystals

Interference fringe periodicity at sub-micron levels is used for fabrication of nano-strucutred 2D PC's. In order for this operation to work, a lithographic technique must then be capable of reaching nano-sized fringe interference. As previously stated in equation (12), fringe period is dependent upon the angle of interference and wavelength of the source laser. Manufacturing optimal interference modulations into the nanometer spectrum requires both a deep UV laser as well as high incidence angle. As the literature shows, the Lloyd's mirror interferometer has the potential for sub-micron periodicity which makes it highly applicable in the thermoelectric field. Thermoelectric devices concentrate on waste-heat-to-energy conversion and temperature regulation [1]. Hochbaum *et al*. observed a substantial increase in thermoelectric efficiency with decreasing diameters of etched silicon nanowire that showed properties superior to grown silicon nanowires [1]. The process for fabricating vertical plasmonic nanowires with uniform diameters, shown in Figures 2.21 and 2.22, requires a combination of metal-assisted etching with laser IL [1]. Here, J. de Boor *et al*. employed a doubled argon-ion laser at a wavelength of 244nm for IL with a Lloyd's mirror interferometer to develop an array of PR posts. The graph in Fig. 2.21(e) represents the various post structure periodicities of the argon-ion 244nm wavelength laser created from an increasing angle of incidence. The slope indicates experimental results performed and that near 100nm fringe spacing is possible at angles of incidence approaching 90°.

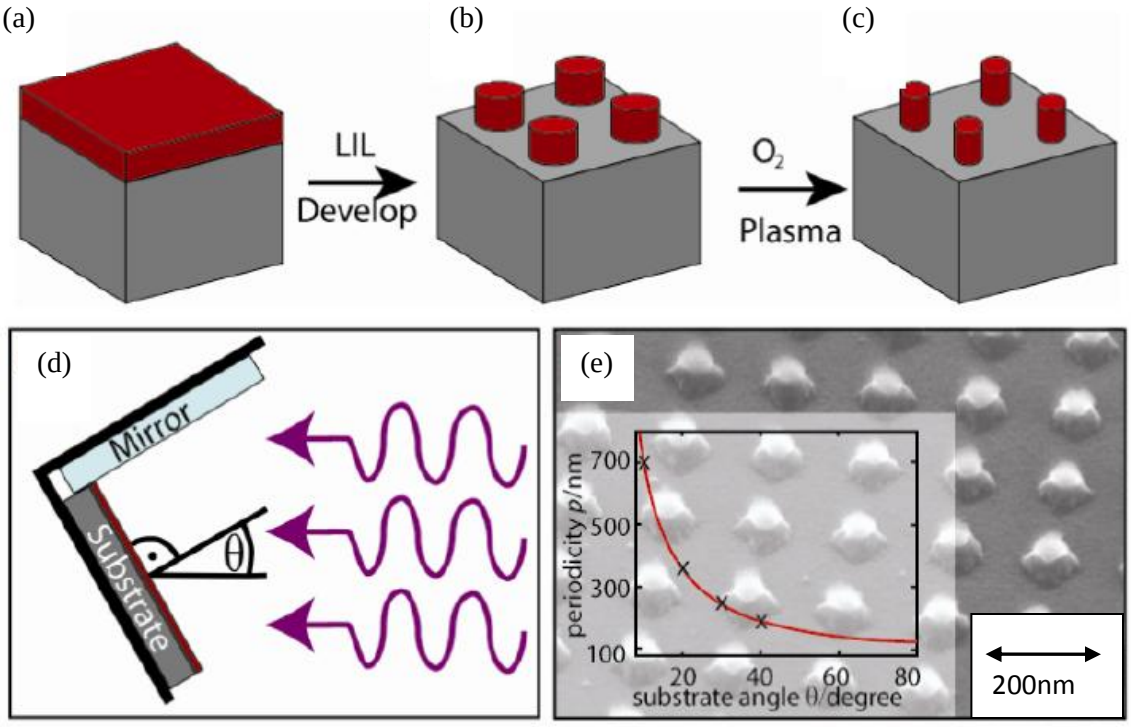

Fig 2.21 (a)–(c) Laser Interference Lithography (LIL) combined with O_2 plasma produced arrays of PR posts. (d) A Lloyd's mirror interferometer allows the periodicity of the PR posts to be determined by adjusting θ, the angle between incident beam and the substrate normal. (e) SEM micrograph of PR posts before O_2 plasma treatment; scale bar 200 nm. The overlay shows the periodicity as function of θ for a wavelength of $\lambda = 244$ nm and the crosses mark experimental results [1].

The metallization process in Fig. 2.22 illustrates the capability of metal assisted etching to form uniform nanowires. To obtain the silicon nanowires, a metal evaporation of 20-nm thick gold is first completed to prepare for a lift-off of the PR. The lift-off removes the PR and leaves a metal film behind on top of the silicon. This is done to replicate the diameter of the resist posts.

In the final step, metal assisted etching dissolves the silicon that is in direct contact with the metal layer, consequently leaving behind silicon nanowires [1].

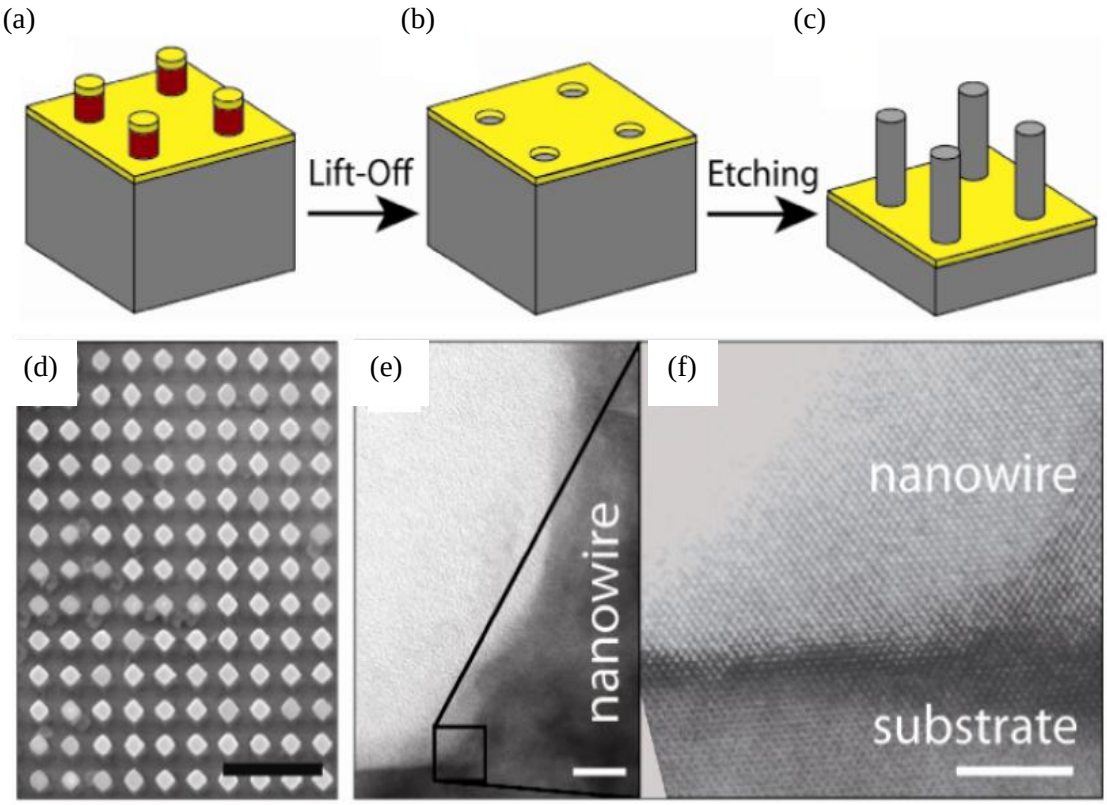

Fig. 2.22 (a) Metal evaporation, (b) lift-off and (c) metal-assisted etching lead to vertically aligned arrays of Si nanowires, shown in (d). The wires have a diameter of around 350 nm, a periodicity of 710 nm and a length of several micrometers. The TEM image in (e) shows the foot of a nanowire and the substrate. The high resolution magnification in (f) proves that the wire and substrate form a single crystal. The scale bars are 2 μm, 10 nm and 5 nm in (d), (e) and (f), respectively [1].

2.5.2 Plasmonics

The study of plasmonics describes light interactions with fabricated metal nano-scale structures that produce electric surface waves known as plasmons. A plasmon is an oscillation of electrons on metal surfaces created from light capture on a metal interface, due to interaction with free electrons. Surface plasmons have gained enthusiasm for the purpose of confining light at a metal-dielectric interface in a sub-wavelength capacity. This process generates intense local electromagnetic fields applicable to photonic devices. The potential for such devices has been demonstrated with enhanced optical transmission through sub-wavelength metal apertures. In this process, light is transmitted through periodic sub-wavelength holes surrounded by materials of various refractive indexes and configurations [6].

2.5.2.1 Enhanced Transmission with Plasmonics

Enhanced transmission relies upon the periodicity of structured apertures for the formation of plasmons from coupling of light at a metal interface [5]. "For a given wavelength, a photon in free space has a wave vector that is always smaller than the corresponding plasmon, which means that the momentum conservation required for their coupling cannot be fulfilled [6]." A periodic grating of slit apertures scatters incident light into various diffraction orders across a metal surface to match diffracted light with its plasmon waves. A Bragg relation, represented in equation (20), describes a new wave vector created from such a grating,

$$k_{sp} = G + k \parallel \tag{20}$$

where k_{sp} is the wave vector of the plasmon mode, G is the reciprocal lattice vector and $k \parallel$ is the in-plane vector component of incident light. From diffraction at the input aperture of hole arrays, light is coupled into plasmon modes and then decoupled at the exit side into freely propagating light. The consequent coupling of plasmon modes enhances the electromagnetic field above the holes and increases the probability of transmission from tunneling. The excited surface plasmons display peak wavelengths (λ_{sp}) within a transmission spectrum predicted by

$$\lambda_{sp} = \frac{P}{\sqrt{i^2 + j^2}} * \sqrt{\frac{\varepsilon_m * \varepsilon_d}{\varepsilon_m + \varepsilon_d}} \tag{21}$$

where $\varepsilon_m$and $\varepsilon_d$are the dielectric constants of the metal and the adjacent medium, respectively; i and j represent the orders of scatter from the array, and P is the lattice constant. This equation implies that the period and the dielectric constants of the interfaces are adjustable. Therefore, it is possible to tune the peak wavelengths of surface plasmon modes. Intensity values for periodic hole arrays are shown in Fig. (2.23) for apertures surrounded by asymmetric (Fig. 2.23(a)) and symmetric (Fig. 2.23(b)) refractive indices. Clearly, the transmission intensity is much larger for apertures in contact with materials of matching refractive index [6]. Further implementation of this relation can be applied to other plasmonic structures to control transmitted light existence by enhanced transmission methods.

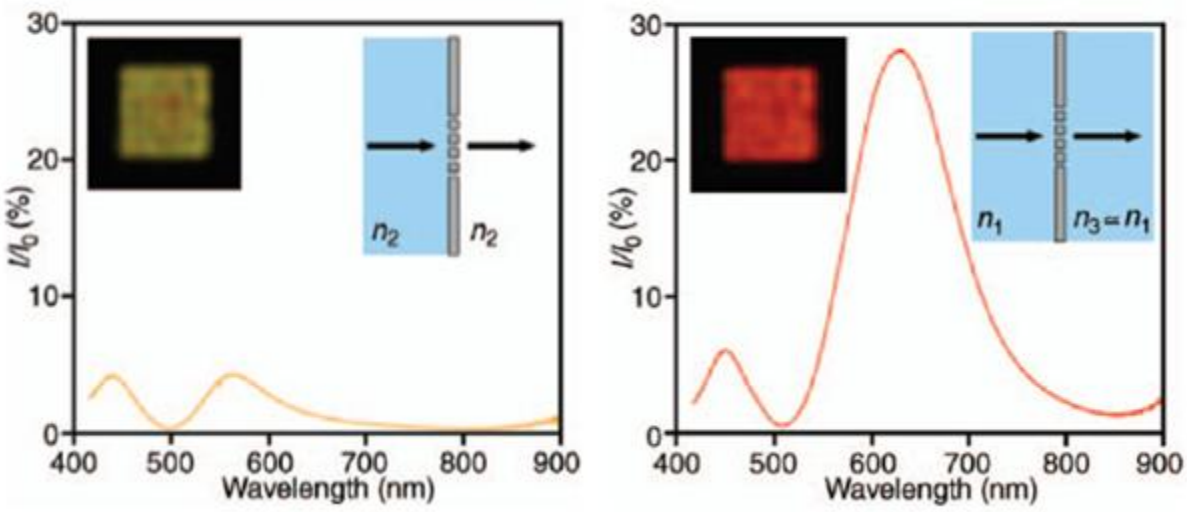

(a) (b)

Fig. 2.23 Normal incidence transmission spectra and images (insets) of a hole array (period, 250 nm; hole diameter, 130 nm) fabricated in a 200-nm-thick Ag film evaporated on quartz substrate (refractive index n_1=1.46). (a) Exit surface in contact with air (n_2=1). (b) Exit surface convered with a film of glycerol (n_3=1.47) [6].

2.5.2.2 Directional Transmission

Standard electromagnetic theories state that light diffracts in all directions from sub-wavelength holes. In contrast, enhanced transmission in single-slit plasmonic structures (Fig. 2.24) can concentrate transmitted light into a diverging beam by surrounding the opening with an appropriate grating on the exit side of the metal interface. Hence, the decoupling of surface plasmons into a material with certain refractive index can be used to confine the diverging beam.

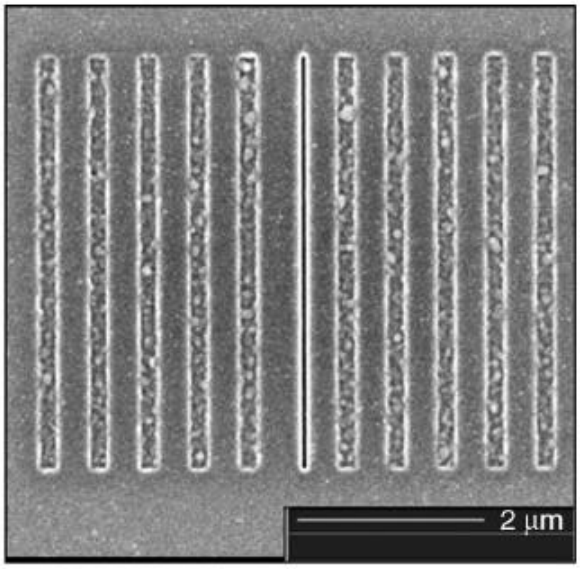

Fig. 2.24 Electron micrograph of a slit surrounded by periodic corrugations in a Ag film (slit width, 50 nm; groove period, 600 nm) [6].

Figure 2.25(a) shows a measured intensity of angular divergence for a slit surrounded by periodic corrugations on both the input and output sides. The input side corrugation couples the incident light, while the output side controls the beaming. Simply changing the refractive index on the output surface changes the beaming pattern, as shown for maximum transmission in Figure 2.25(b). "One can therefore imagine controlling the output beam direction by using a liquid crystal whose index can be varied by applying an electrical potential, as has already been demonstrated for switching the transmission intensity in hole arrays [6]."

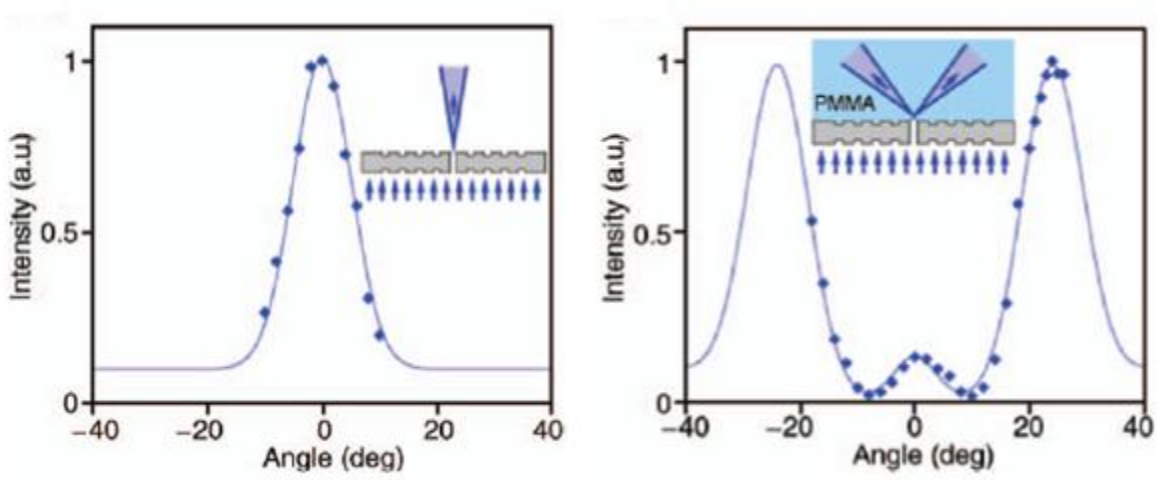

(a) (b)

Fig. 2.25 Angular transmission-intensity distributions of a slit (width, 50 nm) in a Ag film surrounded on the input and output sides by corrugations of the same periodicity (P = 600 nm): (a) with both interfaces surrounded by air and (b) with one interface covered with a thin film of PMMA. Both measurements are at the same wavelength of 690 nm, which corresponds to the longest wavelength transmission peak. The incident light was normal to the surface, whereas the transmission collected at various angles [6].

2.5.2.3 Plasmonic Absorption

Contrary to enhanced transmission, absorption characteristics can be applied to plasmonic structures to produce a perfect blackbody. Kirchhoff's definition of the transmission and absorption relationship states that an object which absorbs all light is known as a blackbody. A perfect blackbody absorbs light radiation at any wavelength and all incident angles while not producing reflected or transmitted light. Blackbodies are currently made from graphite or material covered with black paint that contains graphite particles. Although plasmonics are made with metal surfaces, which reflect most light, the properties of the metallic films can be altered to

match blackbody surfaces by manufacturing an appropriate refractive index. The excitations of surface plasmons to change physical properties of periodic metallic structures make it possible to achieve perfect absorption. Metallic gratings can act as perfect absorbers when Bragg resonances occur to transform incident light into surface plasmons, consequently converting light energy into thermal energy. It has been found that nanostructure metallic gratings with deep height modulations and tuned refractive indices guarantee strong light absorption. Take, for example, a gold plasmonic nanostructure blackbody made of 90-nm gratings. It was experimentally demonstrated to absorb 97-99% of light in a wavelength range of 240-550-nm at incident angles of 0-75° for both TE and TM polarized light [12].

To produce a blackbody it is necessary to develop a coating layer with the best absorbing characteristics (Fig. 2.26). In order to understand absorption of the designed system, consider Fig 2.26(a) of a thin coating layerof thickness, *d*, of the refractive index, *n*, and absorption coefficient, *k*, in $N = n + ik$. "The combination of n ≈ 1 and small *k* provides almost total absorption of light in the covering layer when *d* is much larger than the wavelength of light, λ. The fact that n ≈ N_{air} guarantees the absence of reflection from the first interface and the imaginary part of the refractive index assures the total light absorption in the covering layer provided,

$$2\pi kd/\lambda \gg 1 \qquad (22)$$

Fig. 2.26(b) shows the absorption coefficient of the coating layer of the thickness d = 140nm as a function of n and k. It is clear that one can obtain absorption at the level of 90% in the absorbing layer at the n = 1.3 and k = 0.5 for λ = 400nm. Therefore, the layer with the index of refraction N = 1.3+0.5i would guarantee a very strong absorption of visible light [12]."

Although materials with a refractive index such as the one just described are difficult to find in nature, optical materials with this desired index can be found upon further investigation into metamaterials. Thus, a metal nanostructure with a specific geometry could be fabricated to tune refractive indices to values that would guarantee strong light absorption. Such a structure is depicted in Fig. 2.26(c) and was made of deep gold gratings deposited on Poly-methyl-methacrylate (PMMA). The metal nanostructure has a thickness of about 100 nm and can be used as an effective antireflective and absorption coating layer that possesses the capability for strong light absorption within the UV and visible spectrum. By adjusting the width of the gold nanostructures, the reflection and transmission spectrum can be controlled for both TE and TM polarization. The birefringence of this device therefore indicates potential usefulness as a reflection polarizer [12].

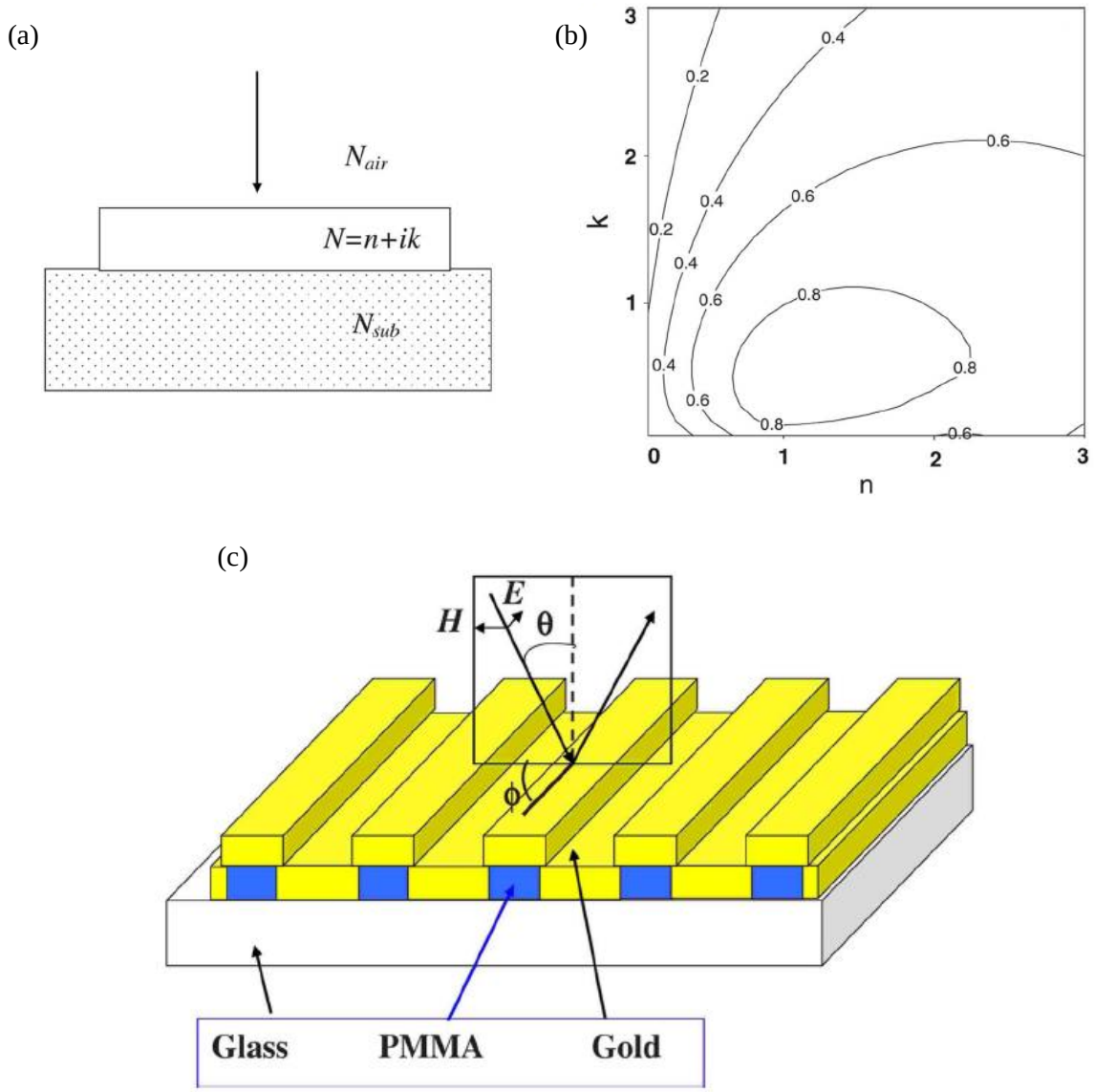

Fig. 2.26 Schematics of plasmonic blackbody. (a) Schematic view of the coating layer on a substrate. (b) A contour plot of the absorption coefficient in *n*-*k* coordinates. (c) The geometry of a 1D sub-wavelength grating [12].

2.6 Chapter Conclusion

The continued growth of the electronics industry is in direct result of the capability to transfer smaller and smaller circuit patterns onto material wafers. This chapter has been presented as the foundation for the following research within this document. It focused on optical laser theory for the development, design, and fabrication of optical devices. The mathematics for the different types of interferometers is quite congruent and limited only by optical design. The applications of photolithographic fabrication have been key enablers for the continued growth of the technology. Among the promising devices are photonic crystals and plasmonic structures, which demonstrate unique optical properties governed by specific geometric features. These devices have demonstrated aspects that are crucial to understanding the potential of laser interference lithography and the capabilities the technology possesses for advancing metamaterial devices.

III. Equipment, Measurements, and Procedures

This chapter describes the equipment, measurements, and procedures used in this effort. A description of the equipment used in this research pertaining to both optical and clean room tools will assist in outlining the measurement methods. For each experiment, schematics will illustrate the types of optical interferometers used in making IL and a detailed description of clean room techniques will be presented. Finally, the lithographic procedures for developing a fabrication recipe will be explained.

3.1 Optical Equipment: Multimode Laser

This section gives a description of the main monochromatic light source used for creating IL in this study. The Kimmon Koha Helium-Cadmium laser operates at duel wavelengths of 325nm and 442nm. For the purposes of photolithography, UV light sources are the most prominent for optimizing interference fringe period into the sub-wavelength spectrum. Thus, all measurements and experiments in this study were performed using the 325nm beam at an unchangeable output power of 35mW. The output beam has a manufacture specification diameter of 1.47mm, a short coherence length of 4in, and functions at a TEM multiple-mode. The multimode beam profile shown in Fig. 3.1 was mapped with, (a) - (b) knife-edge profile and (c) Coherent Beam-code 6.2 software package. The measured 325nm beam diameter was 1.2mm as depicted in Fig. 3.1(b). Fig. 3.1 (c) is a modified illustration of the beam profile to express the distinction between the manufacture diameter specification and the measured beam diameter. This discrepancy will affect the overall intensity distribution of the interference pattern as discussed in Chapter IV.

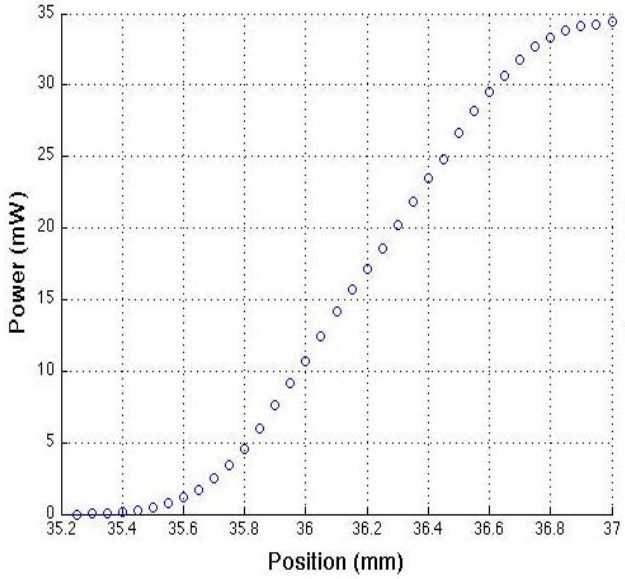

(a)

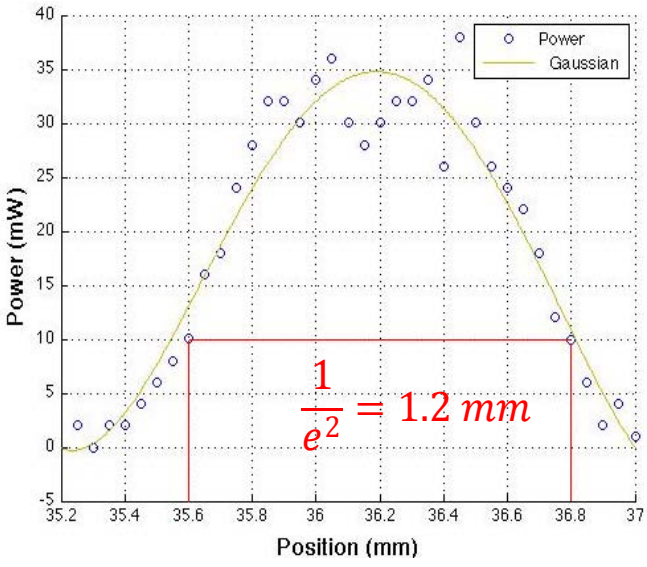

(b)

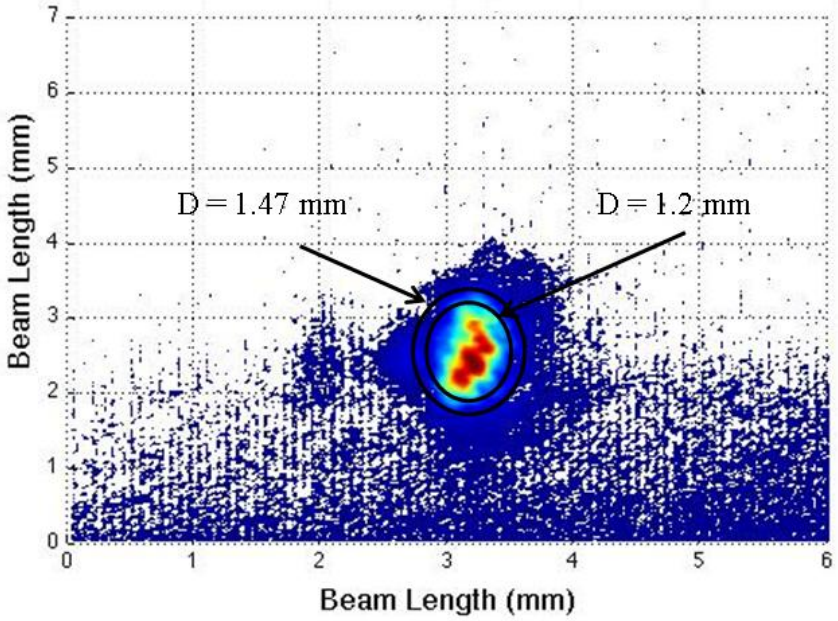

(c)

Fig. 3.1 Kimmon Koha HeCd 325-nm multimode laser beam profile. (a) Knife-edge power plot of the 323nm laser beam. (b) Derivative of the knife-edge power plot. It is the beam profile in the x-direction. (c) The Beam-code 6.2 graph of the 325 nm laser profile which shows the distinction of the manufactures beam diameter vs. the measured beam diameter.

A uniform Gaussian laser is ideal for IL, so a spatial filter was considered for use to eliminate the higher order wave modes of the UV laser. Using equations (16, 17) with $\lambda = 325$ nm, $f = 20$ mm, and $D = 1.2$ mm, a 10-μm pinhole was calculated as the best aperture for filtering the multiple mode beam. With a "clean" beam now radiating from the pinhole, its divergence was collimated to measure an accurate output power. A very low power of 10 μW was measured at the central lobe of the resulting airy pattern, which is where the beam carries the most uniform intensity distribution. Since this reduction in power is unacceptable for interference lithography application as discussed in Chapter IV, the remaining experiments described herein do not adopt spatial filtering of the Kimmon Koha UV laser beam.

3.2 Clean Room Materials and Equipment

3.2.1 Materials: Substrate and Photoresist

Germanium was one of the first materials used in semiconductor fabrication dating back to the first transistor in 1947. However, in the 1960s, silicon replaced germanium because of several dominant advantages. For example, silicon has a wider band gap than germanium, meaning silicon devices are capable of operating at higher temperatures. Perhaps the most important aspect of silicon is its low-cost and elemental abundance [13:2]. Silicon served as the substrate of choice in this study for these very reasons.

The PR selection for this study was based on its potential for meeting the demands of sub-wavelength IL. S1818 and S1805 positive resists were used for the strict purpose of acquiring 100-nm interference fringe spacing; however, the spin coat ratio data presented in Fig. 3.2 does not support a process for manufacturing samples to accept nano-scale IL. Fig. 3.2 plots the

various spin coating rates to produce specific S1800 series PR thicknesses. As the spin speed increases, the thickness of the resist film decreases. Photolithography at the nanometer scale traditionally requires a 2:1 fringe period to PR thickness without the need for an adhesive support layer between the substrate and PR layers. This ratio assures that the PR fringe walls do not topple over themselves after resist development. Based on the thickness limitation for S1800 PR, a process for spin coating silicon samples was devised to support the abilities of each individual interferometer, which is discussed in further detail within the respective IL experiment sections (3.3.1 and 3.3.2).

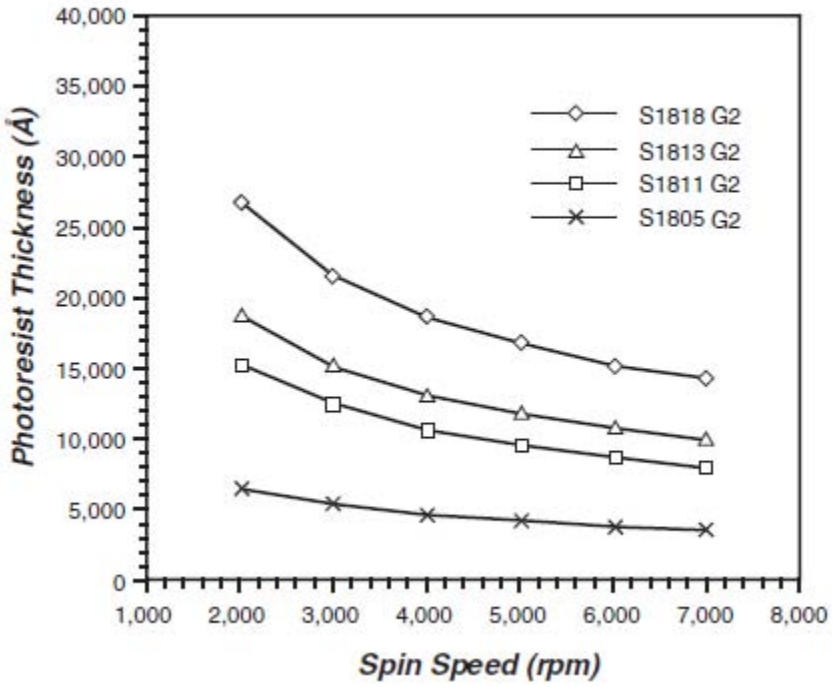

Fig. 3.2 S1800 series plot of PR spin coating speeds. The spin speed application of PR on a substrate determines the resist thickness. Note that resist thickness limitations of S1818 and S1805. S1805 resist is more suitable than S1818 for creating interference fringes into the 100-nm range [18].

3.2.2 Clean Room Equipment: Mask Aligner, Surface Profilometer, SEM

This section describes the clean room instruments used to view and verify experimental fabrication results. The Karl Suss MJB-3 mask aligner is an instrument used in traditional photolithography to transfer mask patterns to PR. The mask aligner used in this study served as a tool to gauge PR thicknesses on a substrate to make sure initial coatings of PR were at the predicted levels for the IL experiments. In this process, half of a newly PR coated substrate was exposed under UV light, while the other half was left unexposed. The exposed region was then developed away, leaving the exposed region of PR to be fed through a surface profiler. A surface profiler is designed to measure feature sizes and in this case, the thickness of the PR layer.

The Alpha-Step IQ surface profiler uses profilometry to measure film thickness. In this technique, a stylus drags across a film surface of step features. When the stylus encounters a feature, a signal variation indicates the feature height. Fig. 3.3 shows a schematic of the profilometer. This instrument has the ability to view uniform features from 5μm down to 100nm, but is recommended only for uniformly structured samples; otherwise, the stylus will not be able to measure feature sizes accurately [13:56].

The preferred method for viewing samples with sub-wavelength features sizes is with a scanning electron microscope (SEM). Unlike optical microscopes, the Hitachi S-4700 SEM is able to view sample features down to 1.5 nm. An SEM uses electrons to illuminate samples as opposed to visible light used in optical microscopy. Since the wavelength of electrons is smaller than that of visible light, an SEM is capable of imaging at much higher magnification but with a consequence. At higher magnification, the samples will experience a charging affect from increased electron flow making PR samples susceptible to overcharging. To combat this effect, a

100-angstrom layer of gold was sputtered over all samples before being viewed with the SEM. The gold layer acts as a conductor for the increased flow of electrons at high-resolution. Instead of overcharging the resist structures, electrons were conducted at the gold layer so that the patterned features were not destroyed.

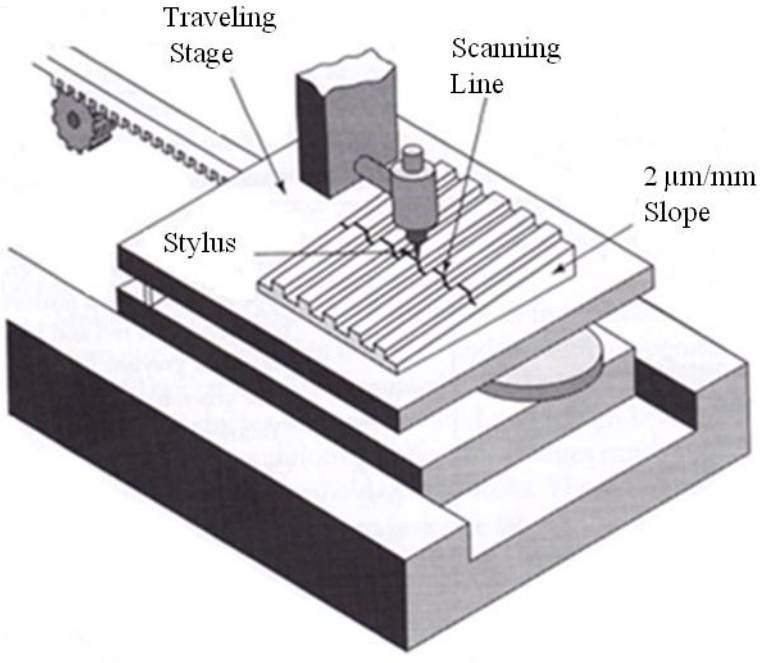

Fig. 3.3 Schematic drawing of a surface profilometer [13:56].

3.3 Procedures

The following section describes the experimental procedures done in this study with both the Michelson and Lloyd's mirror interferometers. The Michelson experiment was done as a trial process to develop a proof of concept for IL. The Lloyd's mirror experiment, however, is an attempt to study the limitations of IL with the equipment presented, and more importantly, construct a fabrication template to produce uniform interference fringes on a sample of PR.

3.3.1 Michelson Experiment: Setup and Measurements

The Michelson interferometer built for this study followed the schematic in Fig. 3.4. It consisted of a beam expander, shutter, amplitude-splitting interferometer and a sample holder. The beam expander, located between the laser source and the interferometer, is comprised of both bi-convex and plano-convex lenses. The purpose of the beam expander is to magnify the source beam of 1.2 mm to 12 mm (0.6 in) to allow maximum area of exposure upon a sample. The bi-convex lens has a ½-in diameter with a 20-mm focal length and the plano-convex lens has a 1-in diameter with 200-mm focal length. Both lenses are UV fused silica (UVFS) and have anti-reflective coatings (ARC) for a wavelength spectrum of 290 nm-370 nm. The lenses were placed at approximately 220-mm (8.6-in) apart to successfully expand and emit a collimated beam into the Michelson interferometer. The interferometer setup is comprised of a 2-in 50:50 UVFS 250-450-nm coated beam-splitter and two 2-in UV enhanced aluminum mirrors. Lastly, the sample holder was positioned 48 cm from the Michelson to accept incident interference radiation.

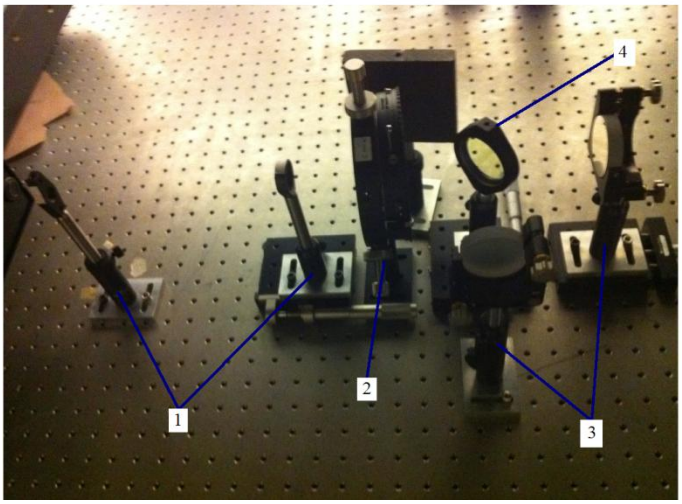

Fig. 3.4 Michelson interferometer consisting of a (1) beam expander, (2) shutter, (3) UV mirrors, and (4) beam splitter.

Silicon samples of 500-µm thicknesses were coated with S1818 resist at 4000 RPM for 30 seconds to yield a 1.8-µm layer of S1818. In order to show the flexibility of the Michelson interferometer, 1D and 2D fringe patterned samples were made using single and multiple exposures, respectively. The Beam-code measurement of the 1D interference fringes before sample exposure for the Michelson interferometer is shown in Fig. 3.5. The fringes are represented by the peaks and troughs of interference in the red and blue regions, respectively. Given this data, an exposure dosage of 173mJ/cm^2 was estimated in conjuncture with the exposure dosages plotted in Fig. 3.6, yielding an exposure time of 17.8 seconds. The plot in Fig. 3.6 represents the approximate exposure dosages of specific resist thicknesses for S1800 series PR. The graph varies with no correlation to a defined sequence or set of equations and is not applicable to the research done herein. However, the purpose for the presentation of Fig. 3.6 is to

show that an exposure template for exposure dosages of resist thicknesses designed for sub-wavelength IL had to be manufactured through experimentation.

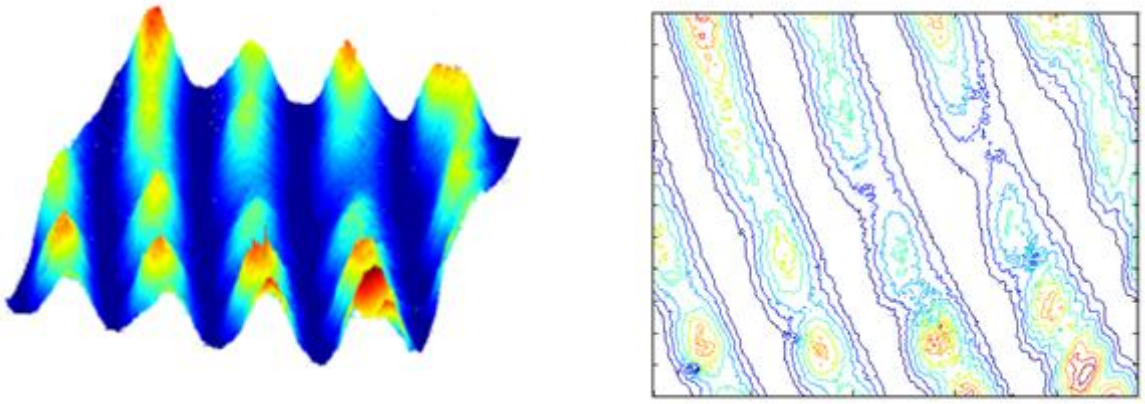

(a) (b)

Fig. 3.5 The (a) 3D plot and (b) contour plot of the measured Michelson 1D interference fringes. The red regions represent the maxima and the dark blue the minima of the fringes.

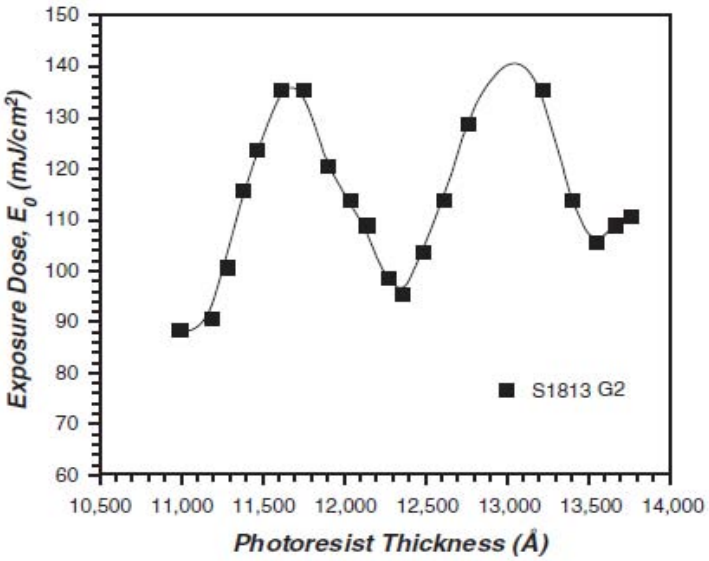

Fig.3.6 A plot of exposure dosages for various PR thicknesses for S1800 series resist. This plot does not show data to support sub-wavelength IL and therefore was not used as a template for creating a fabrication recipe [18].

3.3.2 Lloyd's Mirror Experiment: Setup and Measurements

The Lloyd's mirror optical arrangement shown in Fig. 3.7 consists of the corner cube interferometer described in section 2.2 and the same expander configuration utilized by the Michelson. The Lloyd's mirror mount is comprised of a mirror and sample mount connected atop a rotational stage. The reflecting mirror is a 2-in square UV enhanced aluminum mirror and the sample holder houses a 2-in square vacuum chuck. In order to capture the largest area of interference on samples, there is no separation between the mirror and the sample slide once each piece is in place. An SH05 Beam Shutter system placed at the aperture of the laser controlled the exposure time of the beam incident on a sample. It utilizes a rotary, electro-mechanical actuator to provide sub-millisecond shutter operation. Fig. 3.8 utilizes equation (12) to plot the interference fringe spacing created by the Lloyd's mirror interferometer design given the HeCd UV laser wavelength. In this experiment, the Lloyd's mirror was positioned at 45° to the incident laser beam to produce an interference fringe period of 230 nm.

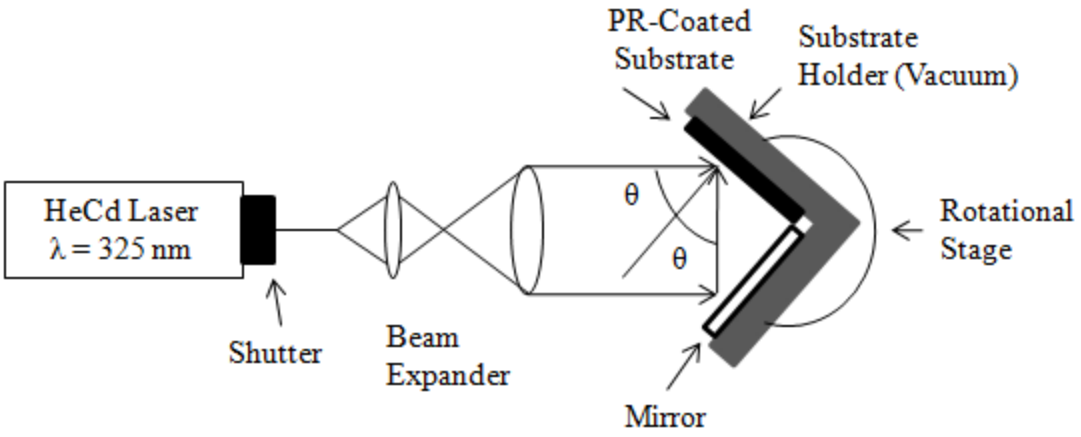

Fig. 3.7 Optical configuration of the Lloyd's Mirror interferometer.

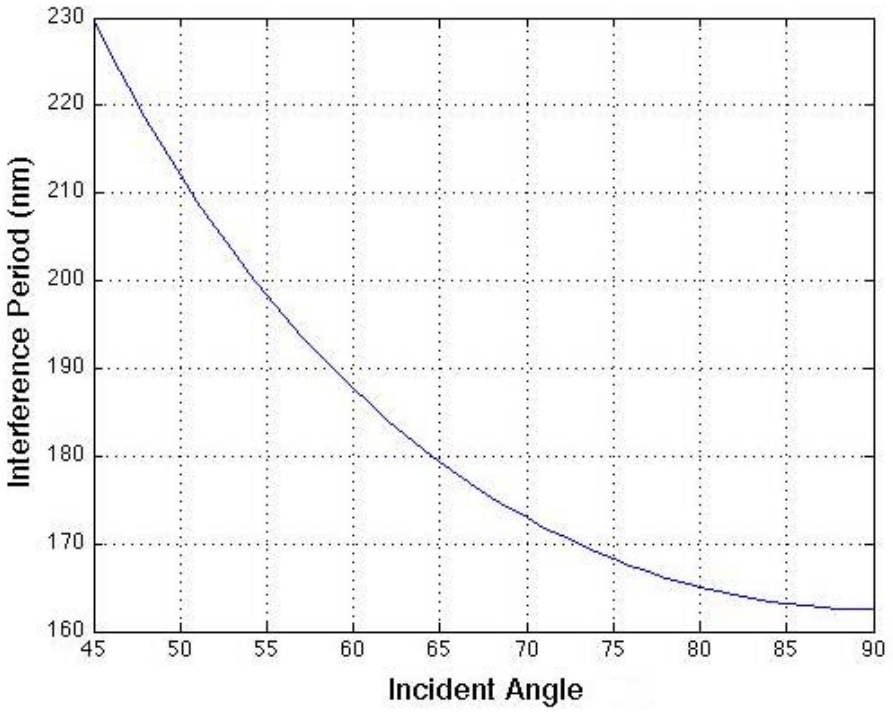

Fig. 3.8 Calculated interference fringe periods of the Kimmon Koha HeCd 325 nm wavelength.

The power collected by a detector aperture area of $\pi(0.475\ cm)^2$ at the Lloyd's mirror was 17 mW, yielding an incident irradiance on the detector to be about 24mW/cm^2. This irradiance was assumed to be uniform over both the mirror and sample of the Lloyd's mirror configuration. The research done with this interferometer only tested interference at 230 nm from a 45° inclination angle as shown in Fig. 3.8. Therefore, the actual irradiance on the Lloyd's mirror was reduced to $24\ mW/cm^2 * \cos(45°) = 17\ mW/cm^2$.The average irradiance was then 2 * 17 mW/cm^2 since the samples are collecting both direct and reflected laser radiation, resulting in an irradiance of 34 mW/cm^2. Finally, the peak irradiance of the maxima interference fringes was

136 mW/cm^2, from four times the average irradiance assuming perfect fringe visibility. However, using equation (14), an OPD = $\sqrt{2}cm$ and the 4-in coherence length of the Kimmon-Koha HeCd laser, visibility could be as low as 0.95, slightly reducing this peak irradiance. By maintaining constant variables such as exposure dosage, PR thickness, PR development, and incident angle, an exposure time of 1 second yielded the best interference fringes with the optical equipment used in this study.

3.3.3 Clean Room Procedures

The clean room segment of this experiment consisted of sample preparation, measurement, and development. In sample prep, 1 cm^2 silicon samples were cleaned by a three-step process. First, the samples were spun at 500 RPM and sprayed with acetone and methanol for 30 seconds followed by a 30-second distilled water (DI) rinse. After solution cleaning, the samples were dried with N_2 and baked on a hotplate for two minutes at 110°C to evaporate any surplus of condensation. Next, the samples were coated with S1805 positive resist at 8000 RPM for 30 seconds to produce a resist thickness of 350 nm measured by the Alpha-Step IQ profilometer. Fig. 3.9 shows an ideal ratio of 2:1 resist thickness as a function of fringe period. For this experiment, a resist thickness of 350 nm was attained in order to maximize the capabilities of S1805 by striving to reach the thinnest deposit layer possible, even though the optical configuration called for a deposit layer of 460 nm for an interference period of 230 nm. Sample development after resist exposure was the last step in the clean room process. Each sample was developed with Microposit 351 5:1 developer for 30 seconds and then rinsed with DI water.

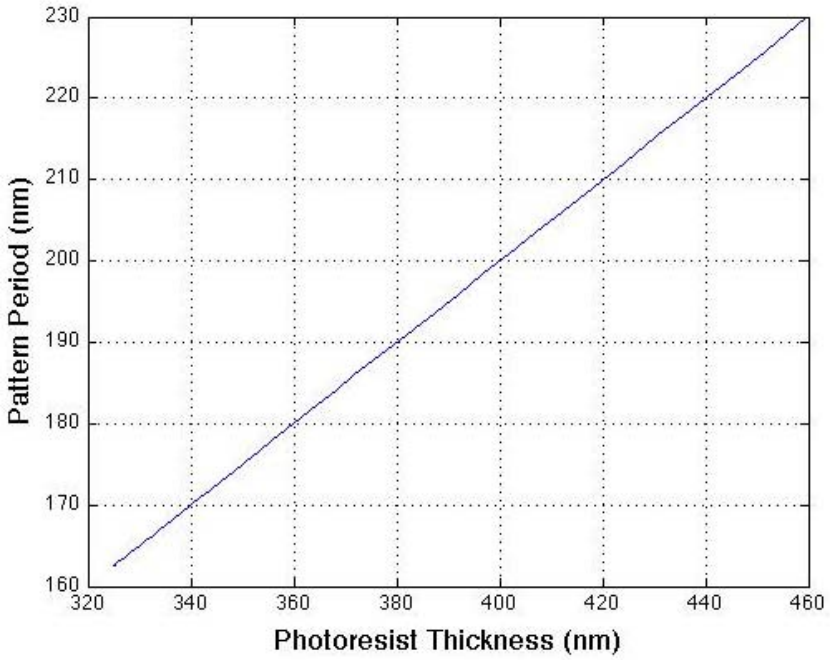

Fig. 3.9 Ideal 2:1 ratio of PR thickness (nm) per interference pattern period (nm) without the need to an adhesion layer.

3.3.4 Sample Characterization

To prove that a 230-nm interference grating was transferred successfully, sample features were verified after exposure with a mathematical rearrangement of equation (19) in the following:

$$\theta_m = \arcsin\left[\frac{m\lambda}{a} + \sin(\theta_i)\right] \tag{23}$$

For $\theta_i = 0 - 90°$, $a = 230$ nm, and $\lambda = 325$ nm, the angle θ_m was calculated as a function of m values. These values represent for the rearranged reflection grating equation that $m = -1$ is the

only diffraction order which can be used for sample characterization. Fig. 3.10(a) plots θ_m as a function of *m* values for $\theta_i = 45°$. The slope indicates that *m* = -1 is able to be viewed at $\theta_m \approx -45°$. By referring to the schematic in Fig. 3.10(b), it is then possible to find a minimal value for θ_i that the *m* = -1 diffraction order can be viewed. Fig. 3.11(a) plots θ_i as a function of θ_m and verifies that θ_i must be 45° to view *m* = -1 diffraction at $\theta_m \approx -45°$. Lastly, Fig. 3.11(b) plots all θ_i to detect the *m* = -1 diffraction order at $\Delta\theta$. These results were roughly verified with the placement of a detector at $\Delta\theta = 10°$ and a scan of the entire reflection angle field., which successfully verified a 230-nm grating of S1805 for $\theta_i = 50°$. It is to be noted that this process is independent of refractive index of the periodic structure because equation (23) is usable regardless of the material index.

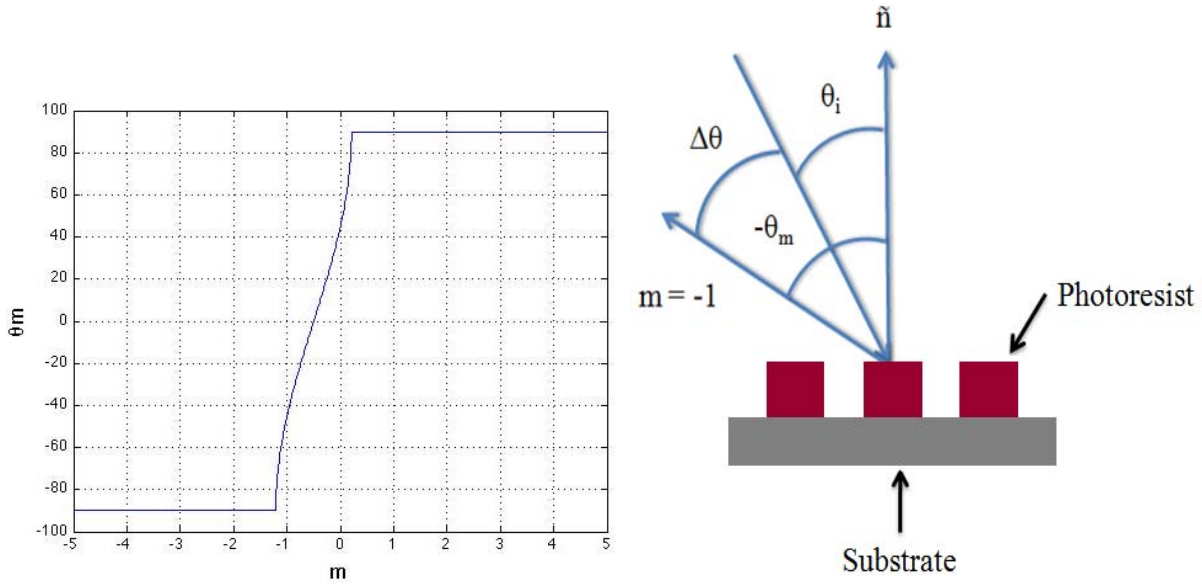

(a) (b)

Fig. 3.10 The reflection phase grating plot for (a) *mth* order of diffraction and (b) schematic of the *m* = -1 diffraction order created by a 230-nm grating produced by the Lloyd's interferometer.

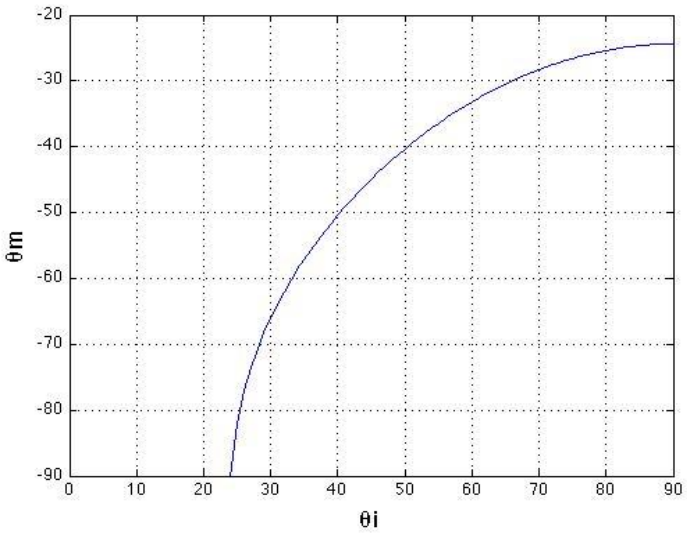

(a)

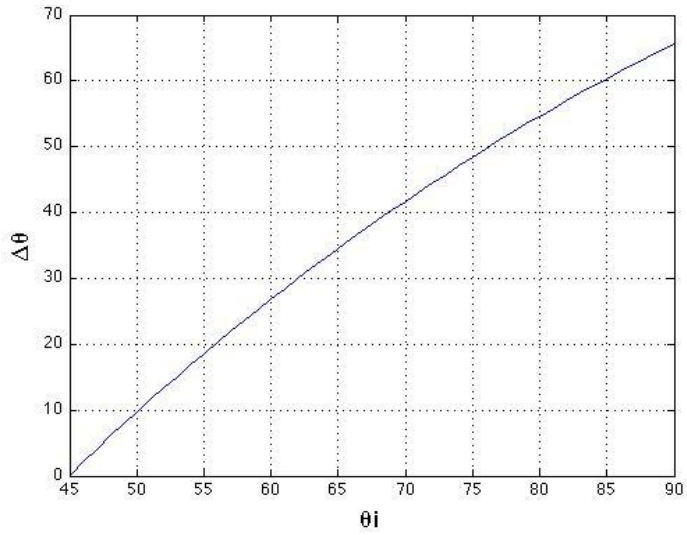

(b)

Fig. 3.11 Reflection phase grating plots for finding, (a) θ_m, and (b) $\Delta\theta$ for given values of θ_i of the 230-nm Lloyd's Mirror Interferometer grating.

3.4 Chapter Conclusion

This chapter described the equipment, measurements, and procedures used in this study. It illustrated the combination of the mathematical definitions of IL and physical measurements. The measurement equipment was introduced for an understanding on the interferometer applications. The concepts of IL presented in the graphs throughout this chapter were demonstrated in the procedures and are fully realized in the results chapter.

IV. Results and Discussion

This chapter focuses on the results from the procedures of both the Michelson and Lloyd's mirror interferometers. The operations of the optical equipment and the interferometers will be discussed and sample results will be presented. The results will provide information about the successfulness of each interferometer and its operational capabilities for the pursuit of creating an ideal fabrication recipe with the equipment provided.

4.1 Laser Profile , Spatial Filtering, and Processing Environment

To create evenly structured high-resolution features by photolithography, typically the source laser beam is described as a TEM single-mode Gaussian because a single-mode laser outputs an equal drop in intensity distribution. A Gaussian laser assures the production of a homogenous interference pattern that can be transferred uniformly into a resist film. A large coherence length is equally as important to photolithography as a uniform intensity profile. Large-scale pattern transfer requires a long coherence length because interference for such an operation produces large OPDs. However, it is important to note that visibility can also be relatively high with short coherence lengths and that only an increasing OPD affects feature resolution. The Kimmon Koha UV TEM multimode laser has an inconsistent intensity distribution, short coherence length, and only one power setting. An inconsistent intensity can lead to erratic and unpredictable exposure dosages while the coherence length limits the ability for large-area interference. In an attempt to produce a uniform intensity distribution, a spatial filter was used to filter out higher order modes to create a single mode Gaussian. This resulted in an airy disk pattern with a central lobe power

of 10 μW. However, a large exposure time of over an hour was the result from such a low power output and no pattern transfer was ever identified at this setting. To produce minimal defects within pattern transfer, IL is based on high exposure dosages at a low exposure time. A long exposure time can leave an optical configuration susceptible to air currents, table vibrations, and a high concentration of dust particles flowing in the path of the laser. In the end, it will be shown the Kimmon Koha HeCd laser used without a spatial filter to maximize sample irradiance was entirely adequate to perform IL because of the small, 1-cm^2 samples exposed. Using equation (14) for fringe visibility, for the Lloyd's mirror setup with OPD = $\sqrt{2}cm$ and L_c = 4in, visibility is always greater than 95%.

IC fabrication facilities require clean room processing, especially in the areas of photolithography. The need for a clean room arises because dust particles can settle on optics and on samples, causing defects, which can result in circuit failure. These types of instabilities can create diffraction rings from laser light bending around particles that reside on optics or from dust on a sample, which can block laser light by acting like a mask. Imagine a hypothetical situation of exposing a 200-mm wafer for 1 min in an air stream at 30 m/min within a class-10 clean room (350 dust particles of 0.5μm and larger per cubic meter). The air volume that goes over the wafer in 1 minute is given by, $(30\ m/min) * \pi \left(\frac{0.2m}{2}\right)^2 * 1\ minute = 0.942m^3$. Then, the number of particles contained in the air volume is 350*0.942 = 330 particles. This is equitable to 82% of 400 IC chips on a wafer infected by at least one particle count of 0.5μm or larger [13:61-62]. Now, if the same scenario is applied to the 1-cm^2 samples used in this study, the air volume over the samples in 1 minute is given by, $(30\ m/min) * \pi \left(\frac{0.01m}{2}\right)^2 *$

$1\ minute = 0.0024 m^3$ and the number of particles contained in the air volume is 350*0.0024 = 0.8 particles. This indicates a relatively small probability of contamination if operating in a class-10 clean room. Unfortunately, the experiments in this study were performed in an optical lab not classified as any level of clean room environment and the results suffered accordingly.

4.2 Michelson Experiment

Feature dimensions for the Michelson interferometer are dependent on angles of interference as stated in equation (12). The smallest feature period possible is always half the wavelength of the source laser because at the largest incident angle of 90°, sin (90°) = 1. Therefore, the fringe period is $P = \frac{325\ nm}{2*\sin(90°)} = 162.5\ nm$. However, it is not possible for the Michelson interferometer to reach such a θ_i because the design is limited by interference created from tilting the reflecting mirrors. θ_i = 0.1° is the largest angle to be expected from the Michelson design, thus producing a pattern period no smaller than 100μm.

The interference fringe patterns transferred to S1818 layered silicon samples for the Michelson interferometer are shown in Fig. 4.1. The 1D fringe array created from a single 18-second exposure has a 120-μm period. Each feature (dark lines) has an approximate width of 100μm. The 1D array in Fig. 4.1(a) is not uniform, but it is representative of a successful trial. If looked at closely, the 1D pattern transitions from thin to thicker features sizes scaling from left to right. Positive resists develop away once exposed, so the thicker resist lines represent underexposure. The thicker regions on the right of Fig. 4.1(a) are areas of underexposure. This could be due to irradiance variations of the Kimmon Koha HeCd laser as depicted in Fig. 3.5.

The 2D PR structure of posts was made from two 17-second exposures and has a 167μm period. The post diameter and height of the posts is 60μm and 0.38μm, respectively. The resulting post heights are shorter than the initial 1.8μm PR layer, which suggests the possibility of overexposure. The fact that the resist structure is that of posts and not a 2D square array confirms overexposure. Overexposure occurred from backscatter of light reflecting from the silicon substrate causing more light exposure to the sidewalls.

These results are indicative of a PR fabrication process not fully realized but do prove photolithographic processes are possible with a Michelson interferometer. The limitation of the Michelson interferometer to conceive only small angles of interference prevented the production of sub-wavelength fringe periods and is the ultimate reason no further research with this design was pursued. Therefore, this experiment can be viewed simply as a proof of concept for developing 1D and 2D PR structures by interference lithography.

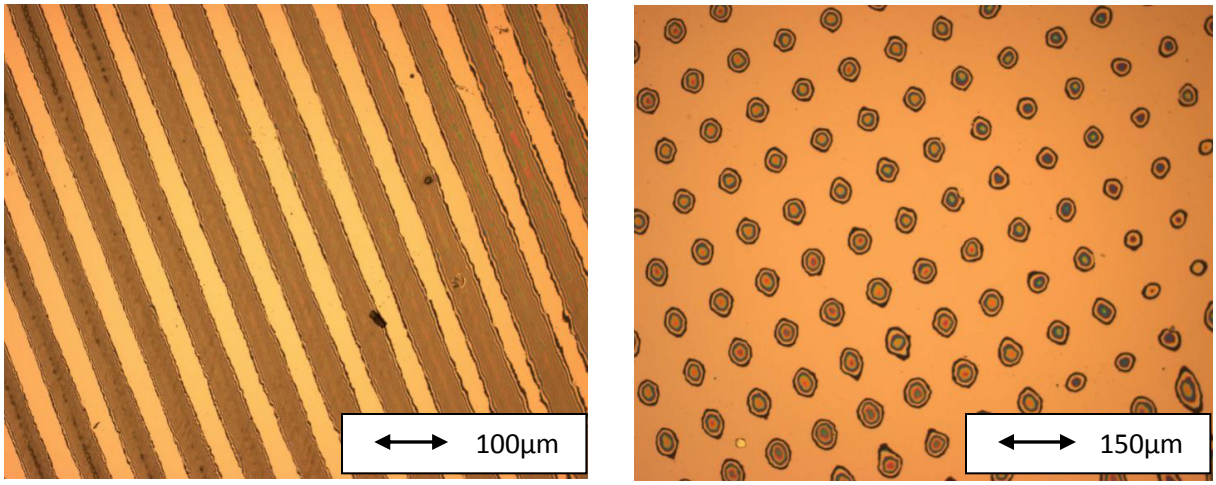

(a) (b)

Fig. 4.1 The Michelson interferometer S1818 samples of (a) 1D fringes with a period of 120μm and peaks 102μm wide and (b) 2D posts with a period of 167μm and dots 60μm wide.

4.3 Lloyd's Mirror Experiment

This section covers the results of the IL fabrication recipe for the LM interferometer. The Lloyd's mirror interferometer was successful in reaching sub-wavelength fringe periods and results correlated with measured data. Through trial and error, an ideal exposure dose of 136mJ/cm^2 for a 350-nm layer of S1805 showed much potential. Since the exposure dose was successful, Fig. 4.2 plots the matching exposure dosages for increasing angles of incidence.

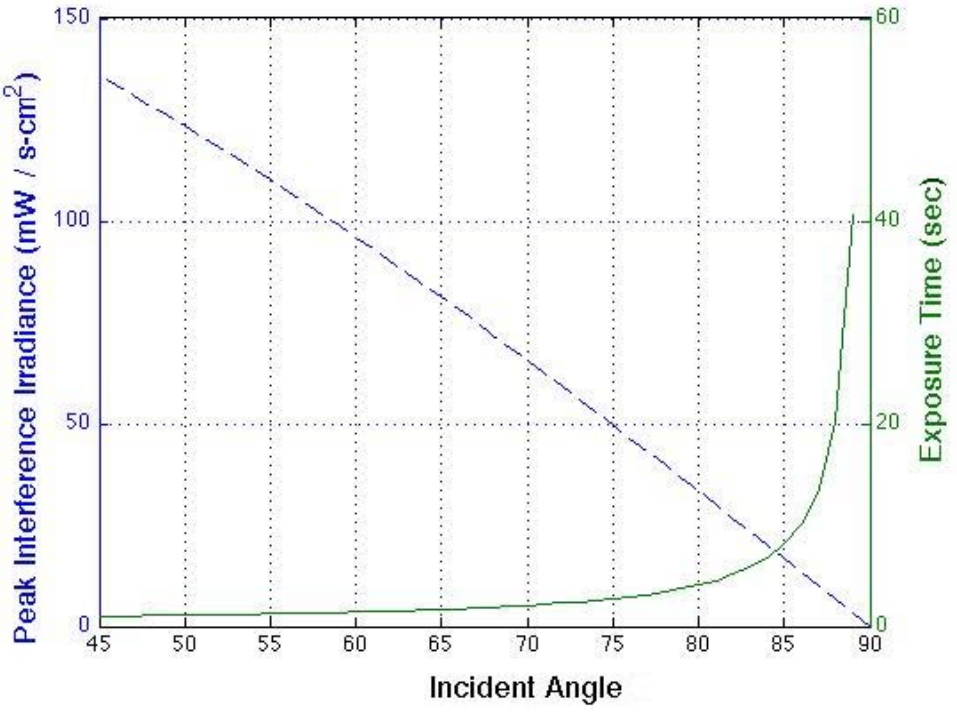

Fig. 4.2 Lloyd's mirror exposure dosages (mJ/cm^2) for increasing incident angle values given an ideal exposure time of 1 second.

The peak irradiance curve decreases with increasing θ_i because the power of the reflected light from the Lloyd's mirror spreads over a larger area. Therefore, the exposure time increases to compensate for the loss in power. For example, at $\theta_i = 75°$, peak irradiance is 50 mW/ cm^2, and exposure time is 2.72 seconds; the exposure dosage is 50 mW/cm^2 * 2.72 sec = 136 mJ/cm^2. Fig. 4.2 assumes all other variables, such as PR thicknesses and laser power, maintain constant values as previously presented.

The SEM results are of one sample from the Lloyd's mirror experiment at multiple regions, all exposed with an irradiance of 136 mJ/cm^2 for 1 second at $\theta_i = 45°$. The white lines in the SEM pictures represent PR features at a period of approximately 230nm. Note that all SEM pictures show multiple vantage points of one sample because entire samples were not exposed. This is due to the beam diameter difference shown in Fig. 3.1. After exposure, each 1-cm^2 sample indicated an exposure across about 75% of the surface area. A beam diameter of 1.47cm was magnified from the manufacture specification of the initial beam diameter of 1.47mm and was theoretically sufficient for exposing a 1-cm^2 at $\theta = 45°$ in the Lloyd's mirror as shown in Fig. 4.3. However, the dissipation in the intensity profile that represented close to 20% of the 1.47-cm beam diameter as shown in Fig. 3.1(c) was representative of the remaining unexposed regions of the samples. This drop in intensity was not enough to create visible interference fringes within those regions of the resist layers. Therefore, it is assumed that the 1.2-cm diameter accounted for the transferred fringe patterns because 1.47cm*(75% exposure area) is 1.1cm, which is approximately the measured 1.2-cm beam diameter.

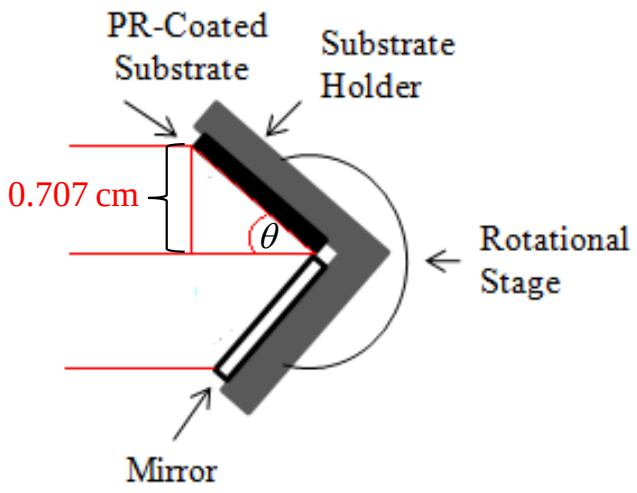

Fig. 4.3 Exposure area of the 1.47cm laser beam. This diagram indicates that half of the beam diameter of 1.47cm is sufficient in exposing an entire 1-cm^2 sample. However, the actual measured expanded beam diameter was 1.2 cm, which did not expose an entire sample.

In each SEM capture, the entire section is exposed to the interference pattern but not all regions show successful pattern transfer and Figs. 4.4 - 4.6 are prime examples of this. The lower resolution fringe patterns in the dark regions suggest (1) the laser interference is not uniform to this extent, (2) the PR thickness is not evenly distributed, (3) dust particles blocked light exposure to the particular area, or (4) poor adhesion of the PR structures to the Si substrate. Again, considering the laser profile of Fig. 3.1, the non-uniformity of the irradiance depicted would be spread across the expanded beam. The full extent of Figs. 4.4 – 4.6 is approximately 12μm, 25μm, and 12μm, respectively. This is less than 2% of the entire beam profile. It is unlikely there would be this kind of intensity variation across such a small region.

The sample fabrication procedure for the Lloyd's mirror experiment coated silicon samples with S1805 resist at a spin speed of 8000 RPM. It is assured that at the center of each sample, there is an even PR coating at this speed and any loss in the consistency of the PR layers resides at the corners of the samples. The exposures shown in the following SEM were performed on or near the center of each sample, and therefore, are representative of interference patterns in a uniform PR deposition. A plausible explanation for the pattern difference over such large distances (μm) is from imperfections on the sample surfaces such as scratches and dust. The dark regions in Fig. 4.5 resemble an area where the PR most likely was scratched off or may not have deposited properly. The more grey regions suggest an area where dust may have settled and blocked some of the laser light, resulting in underexposure. Another justification for the variation of pattern transfer is poor adhesion. Since no adhesion layer was added it is quite possible that the initial PR deposition did not adhere to the substrate firmly. Thus, during exposure the interference pattern did not translate correctly into the PR and most likely evaporated during development processes.

The sample depicted in Fig. 4.7 is a rather odd and unusual result. At first glance, it appears that a diffraction pattern created from either dust or some other obstruction was transferred into the resist film. Judging by the shape of the anomaly, however, it would seem that this conclusion is quite inaccurate. Recall, the Lloyd's mirror was positioned so that light was interfering at a 45° angle, meaning a diffraction pattern would not be as symmetric as the one shown in Fig. 4.7. Instead, the pattern would resemble an ellipse, and therefore, show no similarity to a perfect circle. It is unsure what caused this type of discrepancy, but it could be due to an obstruction in

the layered resist or a defect in the substrate layer consequently affecting the interference fringe structure.

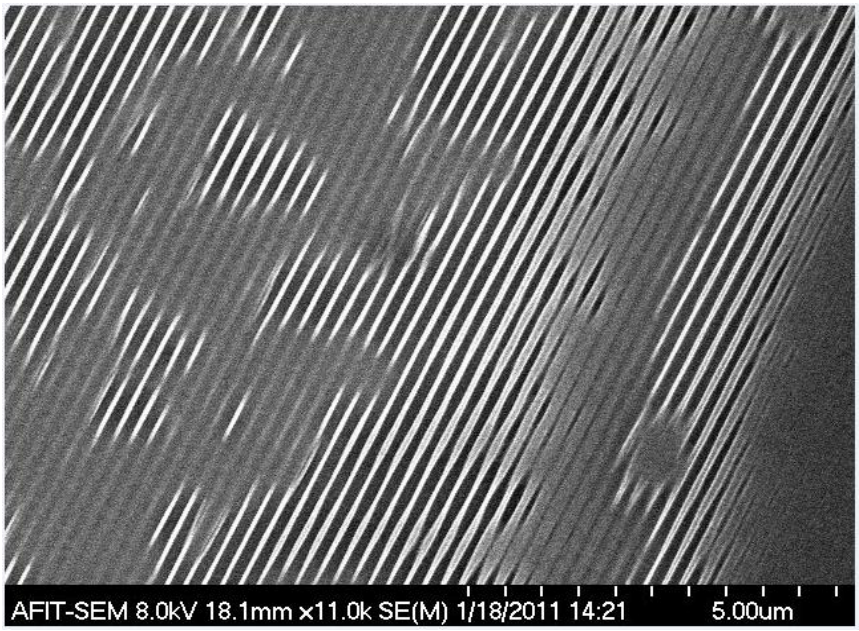

Fig 4.4 Top-down view of 230-nm features in S1805.

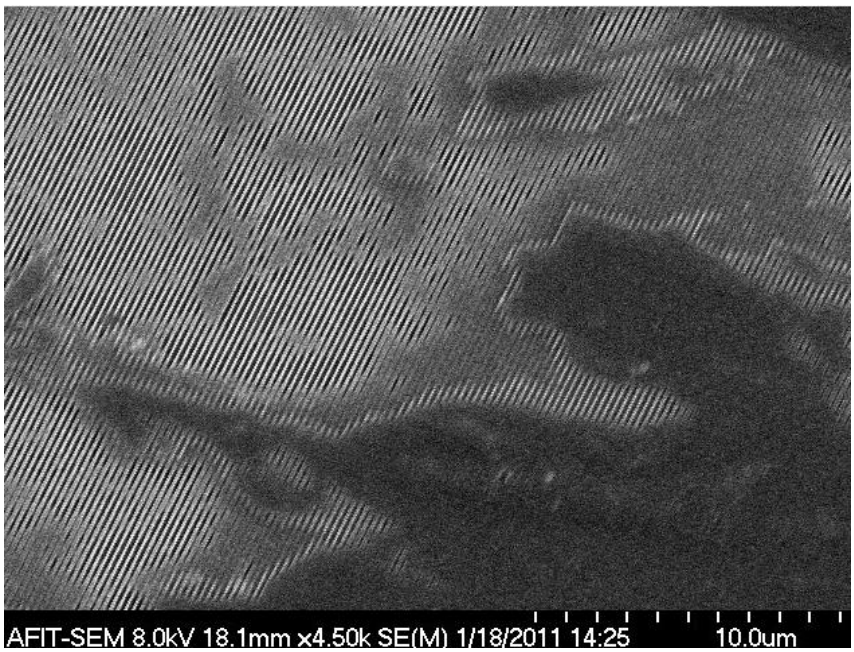

Fig 4.5 Large area capture of 230-nm S1805 features.

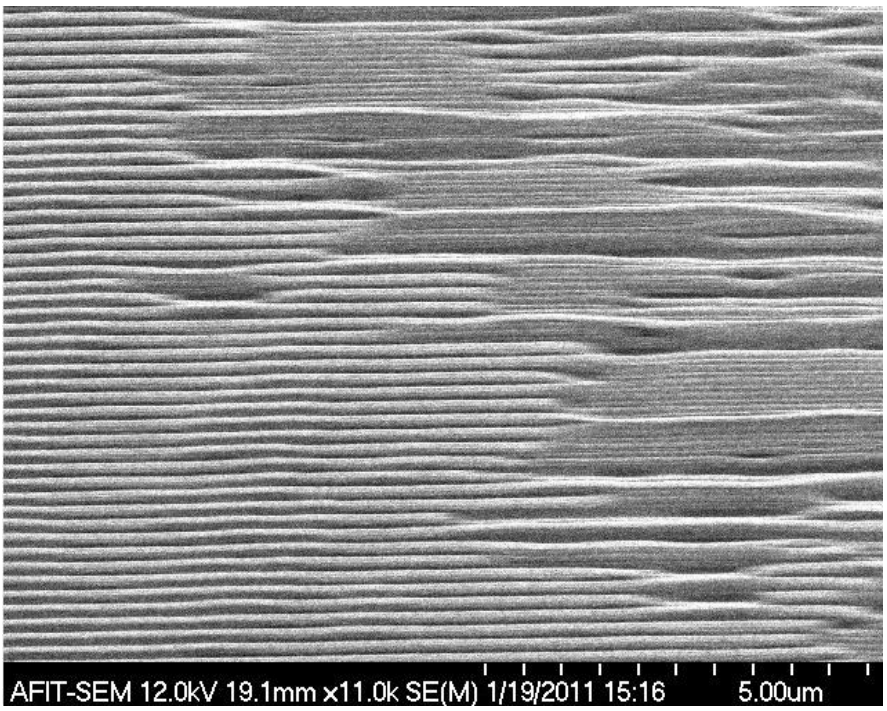

Fig 4.6 Side-view of 230-nm S1805 features.

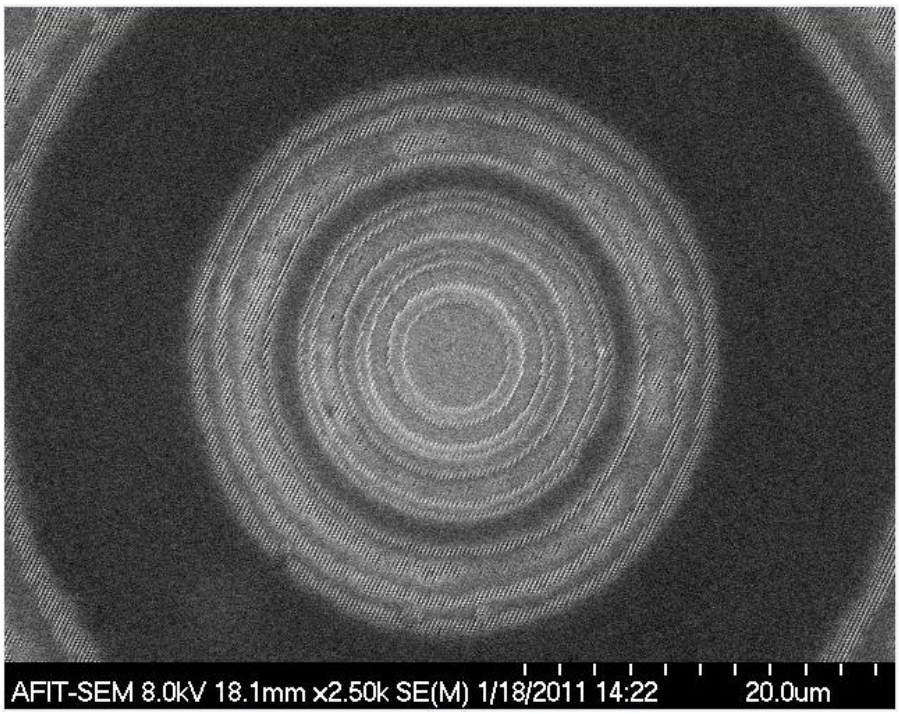

Fig. 4.7 An irregularity within the S1805 feature consistency.

4.4 Chapter Conclusion

This chapter has presented the results from the experiments done in this study. The performance of each lithographic exposure tool was determined by resolution. Resolution is the minimum feature dimension that can be transferred with high fidelity to a resist film. The Michelson interferometer is a flexible design used for developing a basic understanding of IL processing and is not ideal for high resolution structures. On the other hand, the Lloyd's mirror interferometer proved the possibility of sub-micron period gratings. However, the inability to understand the exact cause of the defects within the samples fabricated limited their success in terms of uniformity. Furthermore, an understanding of clean room processes and photosensitive films is essential for optimizing pattern transfer to uncover an ideal exposure method.

V. Conclusion and Recommendations

The objective of this study was an attempt to bring in-house optical nanostructure fabrication methods to AFIT. This entailed a study of optical interferometers and clean room fabrication techniques. The purpose was to gain knowledge about the optical capabilities of each interferometer in order to create the best possible photolithographic system with the equipment available. The goal of the fabrication process was to manufacture a sample development process for optimizing repeatability and throughput within experiments. Laser interference lithography (LIL) provides much potential for next generation optical material fabrication. Small feature sizes, large interference fields, and the production of high-resolution gratings highlight only a few of the accomplishments for developing devices with LIL. The relevance of these abilities is directly associated to photonic crystals and plasmonic structures. The capacity of these devices to both confine and redeploy incident light waves leads to unique optical characteristics, which AFIT is in the position to analyze. The experiments in this thesis fully represent the goals and objectives presented herein.

A photolithographic process transfers patterns of geometric shapes onto a thin layer of photosensitive material. The four things that a photolithography system needs in order to operate efficiently are, ideally, a TEM_{00} source laser, laser interferometer, PR, and sample development process. A device fabrication recipe builds upon the foundation of these four mechanisms and the repeatability of their processes is highly desirable. A TEM_{00} is ideal for IL, but in this study, a multimode laser proved to be sufficient due to small sample sizes. Even with an undesirable intensity distribution and short coherence length, gratings of sub-micron periodicity were achieved with the Lloyd's mirror interferometer. However, further knife-edge measurements of

the expanded beam should be performed to accurately gauge the beam intensity distribution and total power incident on a sample. This could provide accurate irradiance values to yield optimal exposure dosages for highly visible interference fringes. Ultimately, the results presented in Chapter IV were not ideal but they do represent a proof of concept for developing interference fringes at a sub-micron level.

The difficulties within this research dealt with the fabrication processes. A lithographic system should operate in a clean room environment or have tools to maintain cleanliness of the optics and samples. Optical experiments were performed in a lab not classified as any kind of clean room environment and results suffered accordingly. Dust particles jeopardized the cleanliness and overall results of samples under test. With no air regulation, optics and samples were susceptible to complications in interference fringe transfer. To combat this, a container designed to house the optical lithography system should be developed to block dust particles, and a N_2 source could be used to clean samples before and after exposures. A controlled experiment should be performed to test the effectiveness of these alternative methods.

In accordance with clean room standards, an adhesion layer should be added between the substrate and photoresist layers to improve interference pattern transfer regardless of photoresist thickness and fringe period. This will assist etching processes for transferring gratings into underlying layers. If an etching process is to be done, negative photoresist should be used to absorb the interference patterns because chemical etching can be quite aggressive, meaning positive resist structures are unable to withstand such a procedure. Since negative photoresist is highly viscous and bonds together during UV exposure, it is more resilient to etching techniques, making it ideal for manufacturing permanent grating features. Although, negative resists are not

typically employed for nano-scale lithography because the viscosity of the substance hinders it from achieving small initial thicknesses. However, the adhesion layer would be most useful in this aspect to promote large aspect ratios for sub-wavelength fringe spacing.

This research was a stepping-stone for making AFIT self-sufficient in nanostructure design, fabrication, and development. Unfortunately, the time spent at AFIT to fulfill the objectives discussed herein was not enough to present results on a working fabrication procedure. A better, more reliable fabrication recipe is in direct dependence on the environmental conditions of the experiments. This study has identified lithographic results from interference with a multimode laser and concluded that further research in this area concentrate on optimizing clean room procedures to manufacture metamaterial devices.

Bibliography

1. Boor, Johannes de, Nadine Geyer, Jörg V. Witteman, Ulrich Gösele, and Volker Schmidt. "Sub-100 nm Silicon Nanowires by Laser Interference Lithography and Metal-Assisted Etching," *Nanotechnology*., 21(095302), 29. January 2010.

2. Bruek, S.R.J., "Optical and Interferometric Lithography - Nanotechnology Enablers," *Proceedings of the IEEE*., 21(10), October 2005.

3. Byun, Ikjoo and Joonwon Kim, "Cost Effective Laser Interference Lithography Using A 405nm AlInGaN Semiconductor Laser," *Journal of Micromechanics and Microengineering.*, 20(055024), 23. April 2010.

4. Carter, J.M., R.C Fleming, T.A. Savas, M.E. Walsh, and T.B. O'Reilly, "Interference Lithography," *Submicron and Nanometer Structures*, 2003.

5. Degiron, A. and T.W. Ebbesen, "The Role of Localized Surface Plasmons Modes in the Enhanced Transmission of Periodic Subwavelength Apertures," *Journal of Optics A: Pure and Applied Optics*., 7(S90-S96), 20. January 2005.

6. Dintinger, Joše, , Aloyse Degiron, and Thomas W. Ebbesen, "Enhanced Light Transmission through Subwavlength Holes," *MRS Bulletin*, 30, May 2005.

7. Divliansky, Ivan B.,Suzushi Nishimura, Iam-Choo Khoo, and Theresa S. Mayer, "Fabrication of two-dimensional photonic crystals using interference lithography and electrodeposition of CdSe," *Applied Physics Letters*., 79(21), 19. November 2001.

8. Divliansky, Ivan B., and Theresa S. Mayer, "Fabrication of three-dimensional polymer photonic crystal structures using single diffraction element interference lithography," *Applied Physics Letters*., 82(11), 17. March 2003

9. Edmund Optics Inc., "Understanding Spatial Filters," URL http://www.edmundoptics.com/technical-support/lasers/understanding-spatial-filters/.

10. Fernandez, A. J.Y. Decker, S.M. Herman, D.W. Phillion, D.W. Sweeney and M.D. Perry, "Methods for fabricating arrays of holes using interference lithography," *International Conf. of Election, Ion, and Photon Beam Technology and Nanofabrication*., 28. May 1997.

11. Hecht, Eugene. *Optics*. Pearson Education, Inc., San Francisco, CA, 4th Edition, 2002. ISBN 0-8053-8566-5.

12. Kravets, V.G., F. Schedin, and A.N. Grigorenko, "Plasmonic Blackbody: Almost complete absorption of light in nanostructured metallic coatings," *Physical Review B.*, 78(205405), 6. November 2008.

13. May, Gary S. and Simon M. Sze, *Fundamentals of Semiconductor Fabrication*. John Wiley and Sons, Inc., Danvers, MA, 2004. ISBN 0-471-45238-6.

14. Moon, Jun Hyuk and Seung-Man Yang. "Multiple-exposure holographic lithography with phase shift," *Applied Physics Letters*., 85(18), 1. November 2004.

15. Moon, Jun Hyuk, Jamie Ford and Shu Yang, "Fabricating three-dimensional polymeric photonic structures by multi-beam interference lithography," *Polymers for Advanced Technologies*., 17(83-93), 2006

16. Prodan, L., T.G. Euser, H.A.G.M. van Wolferen, C. Bostan, R.M de Ridder, R Beigang, K-J Boller, and L. Kuipers, "Large-area two-dimensional silicon photonic crystals for infrared light fabricated with laser interference lithography," *Nanotechnology*., 15(639-642), 9. March 2004.

17. Quiñónez, F., J.W. Menezas, L. Cescato, "Band gap of hexagonal 2D photonic crystals with elliptical holes recorded by interference lithography," *Optics Express*., 14(11), 26. May 2006

18. Rohm and Haas, "Microposit S1800 G2 Series Photoresists for Microlithography Applications," *Electronic Material: Microelectronic Technologies*., October 2006. URL http: // www.microresist.de/products/room_haas/pdf/Microposit_S1800_G2_Serie.pdf.

19. Su, Hui Min, Y.C. Zhong, X. Wang, X.G. Zheng, J.F. Xu, and H.Z. Wang, "Effects of polarization on laser holography for microstructure fabrication**,"** *Physical Review E*., 67(056619), 21. May 2003

20. Sharp, D. N., A.J. Tuberfield, and R.G. Denning, "Holographic photonic crystals with diamond symmetry," *Physical Review B*., 68(205102), 3. November 2003.

REPORT DOCUMENTATION PAGE			Form Approved OMB No. 074-0188

1. REPORT DATE *(DD-MM-YYYY)*	**2. REPORT TYPE**	**3. DATES COVERED** *(From – To)*
24-03-2011	Master's Thesis	June 2009 – Mar 2011

4. TITLE AND SUBTITLE

Development of Interference Lithography Capability Using a Helium Cadmium Ultraviolet Multimode Laser for the Fabrication of Sub-Micron-Structured Optical Materials

5a. CONTRACT NUMBER

5b. GRANT NUMBER
NA

5c. PROGRAM ELEMENT NUMBER
NA

6. AUTHOR(S)

Crozier, Stanley D., 2d Lt, USAF

5d. PROJECT NUMBER
NA

5e. TASK NUMBER
NA

5f. WORK UNIT NUMBER
NA

7. PERFORMING ORGANIZATION NAMES(S) AND ADDRESS(S)
Air Force Institute of Technology
Graduate School of Engineering and Management (AFIT/EN)
2950 Hobson Way
WPAFB OH 45433-7765

8. PERFORMING ORGANIZATION REPORT NUMBER

AFIT/GE/ENG/11-07

9. SPONSORING/MONITORING AGENCY NAME(S) AND ADDRESS(ES)
Air Force Research Laboratory, Materials and Manufacturing Directorate
Dr. Augustine Urbas
Augustine.Urbas@wpafb.af.mil
Materials & Manufacturing
2977 Hobson Way, Bldg 653 Rm 413
Wright-Patterson AFB OH 45433-7734

10. SPONSOR/MONITOR'SACRONYM(S)
AFRL/RX

11. SPONSOR/MONITOR'S REPORT NUMBER(S)

12. DISTRIBUTION/AVAILABILITY STATEMENT
Approved For Public Release; Distribution Unlimited

13. SUPPLEMENTARY NOTES

This Material Is Declared A Work Of The U.S. Government And Is Not Subject To Copyright Protection Of The United States.

14. ABSTRACT
The goal of this work is to develop unique holograms on a semiconductor-metal thin films to characterize as potential meta-materials. This is achievable by developing a fabrication recipe to include exposure methods, exposure dosages, and material development. This study developed an interference lithography capability at AFIT for the first time with period resolution below 230nm. It also identified initial acceptable photoresist materials and exposure dosages, and a path to follow to optimize this process. The potential impact of this is to make IL a standard in optical meta-material fabrication, which decreases manufacturing time and allows for less error in production. These aspects support a variety of Air Force applications, including high efficiency solar cells and spacecraft thermal management.

15. SUBJECT TERMS
Photolithography, Interference Lithography

16. SECURITY CLASSIFICATION OF:			**17. LIMITATION OF ABSTRACT**	**18. NUMBER OF PAGES**	**19a. NAME OF RESPONSIBLE PERSON**
REPORT	**ABSTRACT**	**c. THIS PAGE**			Dr. Michael M. Marciniak (ENP)
U	U	U	UU	92	**19b. TELEPHONE NUMBER** *(Include area code)* (937)255-3636 x4529, michael.marciniak@afit.edu

Standard Form 298 (Rev: 8-98)
Prescribed by ANSI Std. Z39-18